Incipient wolframite deposition at Panasqueira (Portugal): W-rutile and tourmaline compositions as proxies for early fluid composition

Eleonora Carocci, Christian Marignac, Michel Cathelineau, Laurent Truche, Marc Poujol, Marie-Christine Boiron, Filipe Pinto

Incipient wolframite deposition at Panasqueira (Portugal): W-rutile and tourmaline compositions as proxies for the early fluid composition

Eleonora Carocci[a,*], Christian Marignac[a], Michel Cathelineau[a], Laurent Truche[b], Marc Poujol[c], Marie-Christine Boiron[a], Filipe Pinto[d]

[a] *Université de Lorraine, CNRS, GeoRessources, F-54500 Nancy, France*

[b] *Université de Grenoble Alpes*, CNRS, *ISTERRE, F-38041 Grenoble , France*

[c] *Université de Rennes, CNRS, Géosciences Rennes - UMR 6118, F-35000 Rennes, France*

[d] *Beralt Tin & Wolfram Portugal, 6225-051 Barroca Grande, Portugal & Instituto de Ciências da Terra, Rua Campo Alegre 687, 4169-007 Porto, Portugal*

Email: eleonora.carocci@univ-lorraine.fr

Abstract

The main event responsible for the deposition of tungsten at Panasqueira was closely associated with strong tourmalinization of the wall rocks. Tourmaline is coeval with a W-rich rutile (up to 8-10 wt% W) and both minerals record an early introduction of W in the system, just before the main W deposition. Uranium-Pb dating of the rutile by LA-ICP-MS yielded an age of 305.2±5.7 Ma, which is 6-10 Ma older than the K-Ar age of 296.3±1.2 Ma obtained on muscovite, which was therefore not coeval of wolframite. Major and trace element concentration variations in tourmaline record fluid mixing between two end-members, both considered to be of metamorphic derivation on the basis of REE profiles. We report evidence for a fluid enriched in Co, Cu, Pb, Sc, Sr, V, Cr, Nb, Ta, Sn, interpreted to be of "local" origin, e.g., well-equilibrated with the host formations, and a fluid rich in Li, F, Fe, Mn, W inferred to be of deep origin and related to biotite dehydration. The second fluid carried the metals (in particular Fe and Mn) necessary for wolframite deposition, which were not necessarily inherited from the wall rocks through fluid-rock interaction. Micrometer scale variations in tourmaline and rutile crystal-chemistry are indicative of pulsatory fluid input during tourmalinization.

Introduction

Tungsten (W) in western Europe, was mainly concentrated during the Variscan orogeny. The total endowment is estimated to be 1.1 Mt W. The Central Iberian Zone (CIZ), which contains 210 kt W, is one of the main provinces. Others include the Erzgebirge (270 kt W) and Cornwall (≥425 kt W) (Marignac and Cuney, 2013). The Panasqueira mine in the CIZ, which has been active for more than 130 years, exploits one of the largest W deposits in western Europe, with a total production of 76 kt W since 1934 and estimated total resources of ~ 38 kt W (Almonty, 2016; Vigne et al., 2018), i.e., an *ab initio* endowment of at least 115 kt W.

Since the 1970s, numerous mineralogical, geochemical and fluid inclusion studies have discussed the genesis of the Panasqueira deposit (e.g., Kelly and Rye, 1979; Bussink, 1984; Snee et al., 1988; Polya, 1989; Noronha et al., 1992; Lüders, 1996; Foxford et al., 2000; Polya et al., 2000; Lecumberri-Sanchez et al., 2017; Codeço et al., 2017; Launay et al., 2018). The deposit, which is hosted by the Beira schists, and overlies an inferred contact with a granite pluton (inferred from the presence of a greisenized cupola), is characterized by thousands of sub-horizontal veins filled by wolframite and quartz. Following Kelly and Rye (1979), most studies have concluded that the granite intrusion played a major role in controlling a unique hydrothermal megacycle. Snee et al. (1988) dated muscovite at 296.3±1.2 Ma (2σ), using the $^{40}Ar/^{39}Ar$ age step-heating method, and considered this age to represent the approximate timing of the main W depositional stage, assuming coeval crystallization of wolframite and muscovite.

Recent investigations carried out on the scale of the whole deposit reported observations of mineral sequences synchronous with the incipient opening of the W veins. The fluid inclusion record of the event in which wolframite was deposited (the OSS stage of Polya et al., 2000) was lost due to decrepitation and/or deformation after wolframite crystallization (Cathelineau et al., 2017; 2018; Carocci, 2019), a fact which unfortunately was overlooked by all previous studies. As a result, there is no reliable record of the fluids responsible for wolframite crystallization. A potential way to constrain the composition of these early fluids is to study the crystal-chemistry and trace element concentrations in minerals coeval with incipient wolframite deposition. Here, we demonstrate that tourmaline in the wall rock, and associated rutile, were indeed coeval with wolframite deposition. Both minerals display chemical zoning, taken as proxy for the evolution of the fluid chemistry during their growth. Tourmaline is known to be highly stable under a wide range of physico-chemical conditions (van Hinsberg et al., 2011). Its complex structure inhibits significant element diffusion on available timescales (Hawthorne and Dirlam, 2011) and records changes in fluid chemistry at all stages of crystal growth (Marschall and Jiang, 2011; Sluck and Trumbull, 2011; van Hinsberg et al., 2011). Although several studies of the Panasqueira tourmaline have examined the major element and boron isotope composition (Neiva et al., 2007; Codeço et al.,

2017; Launay et al., 2018), none have investigated the trace element chemistry and the possibility that it could record the evolution of the fluid or change(s) in the fluid source(s).

The main objective of this study was therefore a comprehensive analysis of tourmaline and rutile chemistry in order to constrain the nature of the ore forming fluids. This resulted in a modified conceptual model of the early hydrothermal system at Panasqueira. A subordinate objective was to date the rutile using the *in situ* U-Pb method, in order to constrain the onset of hydrothermal activity and provide a comparison to the published ^{40}Ar muscovite age.

Regional background

Panasqueira is located in the Iberian Massif, which is the southern branch of the so-called Iberian-Armorican Arc (IAA), at the western termination of the Variscan belt. The IAA is an orocline formed in about 10 Ma at the end of the Carboniferous (Weil et al., 2013). The Iberian Massif is subdivided into a number of tectonostratigraphic units (or Zones) (Julivert et al., 1972) delimited by tectonic boundaries (Fig. 1). Most of these terranes are Gondwanian in origin. The Central Iberian Zone (CIZ) is the main unit of a series of autochthonous terranes derived from the Paleozoic Gondwanian passive margin. They were covered by a unique nappe stack (Galicia-Tras-os-Montes Zone and Ossa Morena Zone) (Pérez-Caceres et al., 2017). The CIZ comprises a thick sequence of late Ediacarian-Cambrian metasedimentary rocks (the Schist-Greywacke Complex, or Beira Group) overlain unconformably by the Early Ordovician Armorican Quartzite (Diez-Fernandez et al., 2013).

The tectono-thermal Variscan history of the CIZ, which begins in the Early Carboniferous and ends in the Early Permian, is subdivided into five events, D1 to D5 (Diez-Fernandez et al., 2016, and references therein; Diez-Fernandez and Pereira, 2017). The first event, D1 crustal thickening and stacking of the allochthon, was dated at *c*. 354-347 Ma (e.g., Rubio Pascual et al., 2013). The subsequent D2-D5 evolution was characterized by large-scale crustal melting, resulting from a combination of mid-crustal post-thickening heating and mantle-derived heat input at the base of the continental crust (Pereira et al., 2017). The D2 (*c.* 327-316 Ma) event recorded the first episode of heat input and mid-crustal melting, with the development of migmatite domes (Fig. 1) (e.g., Llana-Fúnez and Marcos, 2007; Diez Fernandez et al., 2012; Rubio-Pascual et al., 2013; Pereira et al., 2017). Associated mafic syn-migmatitic sills and sheet-like bodies of late-kinematic monzogranite and granodiorite (319-316 Ma) are widespread (e.g., Castro et al., 2003; Pereira et al., 2017). The D3 to D5 evolution corresponds to a protracted sequence of episodic intra-crustal transcurrent deformation, initiated at ca. 315-310 Ma by the development of km- to 10 km-sized NW-SE to N-S

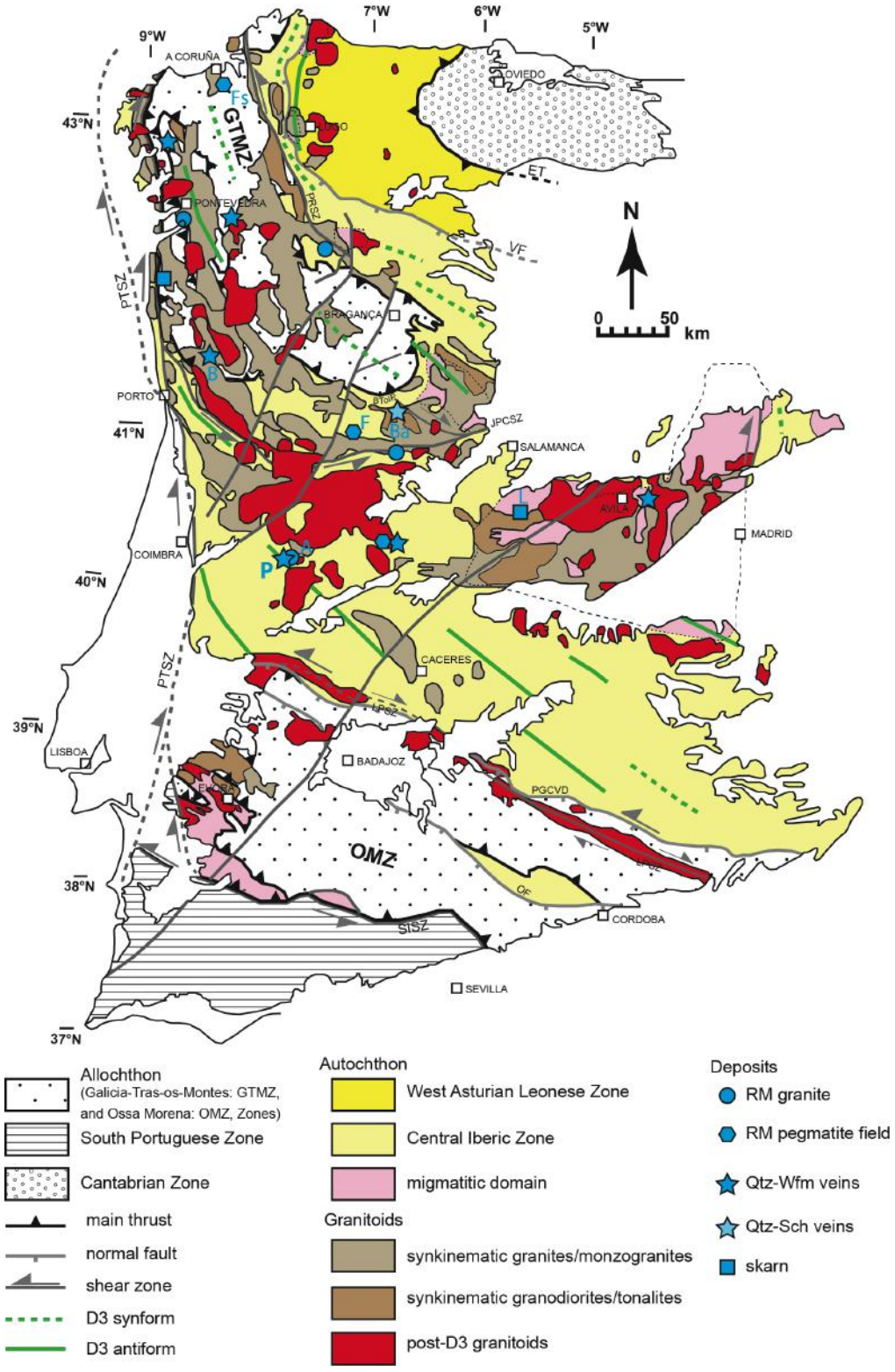

Figure 1. Geologic map of the Iberian Massif, with Panasqueira location. The map is adapted and simplified from Diez Fernandez et al. (2016), with complementary data from Alcock et al. (2015), Llana-Furez and Marcos (2007), Rubio Pascual et al. (2013) and Rubio-Pascual et al. (2016). BToIP: basal thrust of the Iberian Parautochthon; ET: Espina thrust, JPCSZ: D4 Jusbado-Perralva do Castelo shear zone; LPSZ: Los Pedroches shear zone; OF: Onza fault; PGCVD: Puente Genave-Castelo Vide detachment fault; PRSZ: Palas de Rei shear zone; PTSZ: Porto-Tomar D5 shear zone; SISZ: South Iberian shear zone; VF: Viveiro fault

upright F3 folds, with a S3 axial-plane schistosity, followed by D4 (*c*. 309-305 Ma) left-lateral and D5 (*c*. 304-295 Ma) dextral faulting (Diez Fernandez and Pereira, 2017; and references therein). Crustal melting and concomitant mantle-derived heat input continued through D3 to D5, with the pervasive emplacement of syn- to post-kinematic granite plutons, in three pulses roughly coincident with the D3 to D5 events (e.g., Dias et al., 1998; Mateus and Noronha, 2010; Sant'Ovaia et al., 2010; Fernandez-Suarez et al., 2011). Water-absent dehydration melting (incongruent biotite melting) produced cordierite-bearing diatexites in the cores of D2 migmatitic domes (Pereira Gomez et al., 2000). Permian mafic dikes (290-265 Ma) testify to a mantle influence until the very end of the collision (Orejana et al., 2009; Scarrow et al., 2011).

Numerous mineralized systems were active in the CIZ in close association with Late Carboniferous tectonics and granitoid emplacement giving rise to more than 150 peri- and intra-granitic rare metal (Nb-Ta, Li, W, Sn) and shear-zone hosted (Au-Ag-As-Sb-Pb-Zn-Cu) deposits (Tornos et al., 2000; Neiva, 2002; Mateus and Noronha, 2010; Noronha, 2017).

Geological setting and previous work

The Panasqueira W-Cu (Ag)-Sn deposit in central Portugal lies within the Central Iberian Zone (CIZ) (Fig.1), in the core of a late Carboniferous anticlinorium bordered by narrow synclines of Ordovician Armorican Quartzite (Fig. 2-A). The deposit consists of a dense network of sub-horizontal mineralized quartz veins crosscutting the subvertical foliation of the greenschist facies mica-schists of the Beira Schists (Fig. 2-B). These veins crosscut numerous pods and vein-like masses of barren quartz locally named “seixo-bravo” which are probably late kinematic and cover an area of over six km^2; their vertical extent is several hundred meters (Polya, 1989).

A granite body concealed beneath the deposit (Fig. 2-B) was responsible for a 6x3 km metamorphic contact aureole of schists, marked by cordierite-biotite spots and cordierite-andalusite assemblages. These mineral assemblages constrain the pressure to have been less than 300 MPa at the time of emplacement of the Panasqueira granite (Pattison, 2001; Kuhn, 2018). A greisenized cupola at the top of the granite is still observed in some of the galleries. This cupola was described by Kelly and Rye (1979) as having being overlain by a quartz cap, although this has not been corroborated. The greisenized cupola sits atop a sheet-like body of evolved granites that are mainly evident in a few drill holes (Bussink, 1984; De Amorin, 2017), but have been encountered locally in some of the deepest galleries of the mine (LB level, Barroca Grande sector: Lourenço, 2002). The cupola sent out several sill-like apophyses, and towards its base, a matrix-supported breccia formed with large (up to 2 m) joint-bounded hornfels clasts (Kelly and Rye, 1979). The greisenized cupola

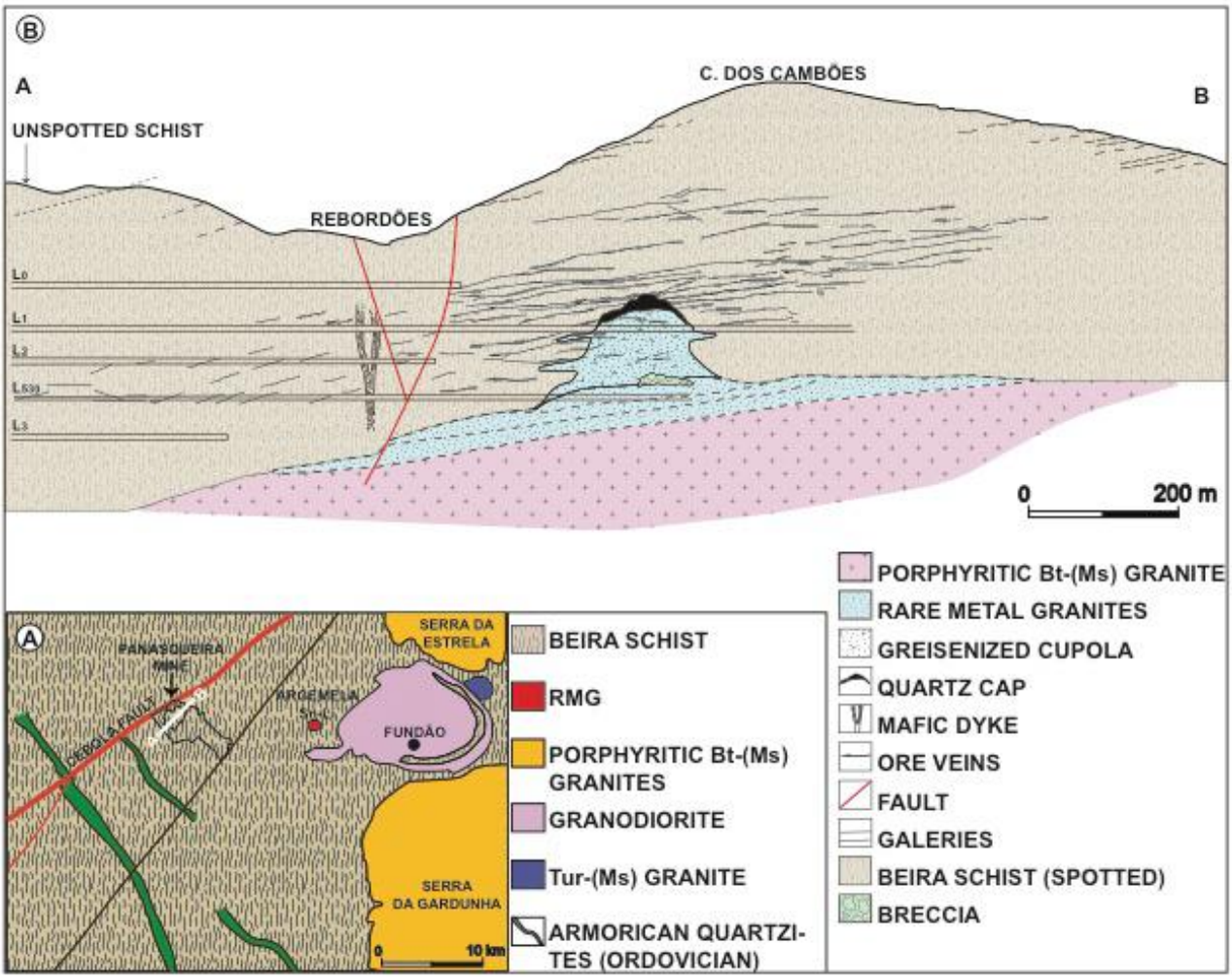

Figure 2. Panasqueira geological setting. **A**. Geologic map of the Panasqueira area (redrawn from Ribeiro, 2017), with location of the cross section in B. Note the tight synform roots picked out by Ordovician quartzites. **B**. Cross section of the Panasqueira deposit (adapted from Bussink, 1984 and De Amorin, 2017)

is cut by the quartz-wolframite veins. The evolved granites are typical of the peraluminous rare metal granite (RMG) family (Linnen and Cuney, 2005), and are albite-rich, displaying typical "snowball" quartz textures. They contain (rare) cassiterite and columbo-tantalite as accessory minerals (Lourenço, 2002; De Amorin, 2017). A porphyritic (K-feldspar megacrysts) biotite-(muscovite) granite (Bussink, 1984) is likely representative of the main granite body responsible for the metamorphic aureole and could be related to the late D3 granites from the nearby Serra de Estrela (Sant'Ovaia et al., 2010) and Serra de Gardunha (Fig. 2-A). According to recent gravimetric data (Ribeiro, 2017), the main Panasqueira granite has the shape of a laccolith, with a flattened top, a NNE striking elongated trend (~6.3×3.8 km) and an average thickness of 1 km, but with a 2 km thick keel. The evolved granites have been dated at c. 290 Ma, by whole-rock K-Ar (Clark, 1970) or Rb-Sr (Priem and Den Tex, 1984) methods. Close to the deposit, the Fundão granodiorite (Garcia,

2004) and the small Argemela RMG intrusion (Michaud et al., 2020) are associated with a quartz-cassiterite vein system (Inverno et al., 2009).

The Panasqueira deposit first attracted research attention in the second half of the 20th century (Kelly and Rye, 1979; Polya et al., 2000, and references therein; Lourenço, 2002; Burnard and Polya, 2004) and continues to be the subject of considerable interest. Jaques and Pascal (2017) and Jacques et al. (2018) addressed the tectonic and fluid pressure conditions required for the creation and opening of the quartz vein system. Lecumberri-Sanchez et al. (2017), using LA-ICP-MS analyses of fluid inclusions, and Codeço et al. (2017), using B-isotope data from tourmaline, addressed the origin of the fluids. Launay et al. (2018) used tourmaline growth features to interpret the direction and velocity of flow of the fluids.

Samples and methods

Our work is based on analyses of >250 samples collected in the late 1970s on levels 0 and 1, in the historical centre of the mine, and in 2015-2016 on levels 0 to 3, to the south-west of the historical zones. Following petrographic examination with an OLYMPUS BX51 (transmitted and reflected light) optical microscope and a VHX-200 KEYENCE numeric microscope, selected samples were studied with a Schottky-FEG (Field Emission Gun) JEOL J7600F scanning electron microscope (SEM) equipped with an SDD-type EDS spectrometer at the GeoRessources Laboratory (Nancy, France). Backscattered electron (BSE) images were obtained after setting the acceleration voltage at 15 kV.

Major-element mineral compositions were determined for tourmaline and rutile using a CAMECA SX100 Electron microprobe (EPMA) equipped with a wavelength dispersive spectrometer (WDS) and a Schottky-FEG (Field Emission Gun) JEOL J7600F scanning electron microscope (SEM) equipped with a SDD-type EDS spectrometer at the GeoRessources Laboratory (Nancy, France). The analytical conditions were a 12 nA current and an accelerating voltage of 15 kV for the EPMA, and a 1 nA current and an acceleration voltage of 15 kV for the SEM, with a counting time of 10 s. The same natural and synthetic oxides and silicate standards were used for the two types of analyses. For tourmaline analysis, these standards were topaz (F), albite (Na), olivine (Mg), orthoclase (Si, K), wollastonite (Ca), $MnTiO_3$ (Ti, Mn) and hematite (Fe). For rutile analysis, the standards were TiO_2 (Ti), Cr_2O_3 (Cr), vanadinite (V), hematite (Fe), $LiNbO_3$ (Nb), $LiTaO_3$ (Ta), cassiterite (Sn) and scheelite (W).

Trace and rare earth elements in tourmaline were analyzed at the GeoRessources Laboratory, using a 193 nm GeoLas Pro ArF Excimer laser at 5 Hz laser frequency, the aerosols being analyzed

with an Agilent 7500c Quadrupole ICP-MS. The analytical settings for laser ablation are detailed in Leisen et al. (2012) and Lach et al. (2013). Laser ablations were performed with a constant fluence of 10 $mJ.cm^{-2}$ and a constant repetition rate of 5 Hz. Helium was used as a carrier gas to transport the laser generated aerosols from the ablation cell to the ICP-MS. Before entering the ICP torch, Helium was mixed with Argon at a typical flow rate of 0.5 $l.min^{-1}$. The hole produced by the laser was 24 µm in diameter, except for REE measurements, for which it was 120 µm in diameter. A peak hopping ablation mode was initiated ~ 20 s after the beginning of signal acquisition, in order to sample the background signal before ablation (used for data reduction), and was stopped after 200 pulses. The return of the background signal to its initial value was checked before ablating a new zone. The NIST reference glasses 610/612 were used as external standards; Si, previously analysed by EPMA, was used as an internal reference. The data were processed using the Iolite software (Paton et al., 2011).

Rutile U-Pb geochronology was conducted by in-situ laser ablation ICP-MS at Géosciences Rennes using an ESI NWR193UC Excimer laser coupled to a quadrupole Agilent 7700x ICP-MS equipped with a dual pumping system to enhance sensitivity (Paquette et al., 2014). The instrumental conditions are reported in Appendix A1, Table A1.The ablated material was carried into helium, and mixed with nitrogen and argon, before injection into the plasma source. The instrument was aligned and calibrated for mass before each analytical session using the NIST SRM 612 reference glass, by inspecting the ^{238}U signal and minimizing the ThO+/Th+ ratio (<0.5%). During the course of an analysis, signals for ^{204}(Pb+Hg), ^{206}Pb, ^{207}Pb, ^{208}Pb, ^{232}Th and ^{238}U masses were acquired.

Single analyses consisted of 20 s of background integration followed by 60 s of sample integration with the laser firing and then a minimum delay of 10 s to wash out the previous sample. Ablation spot diameters of 45 µm with repetition rates of 5 Hz were used for all the analyses. For each analytical session, we used the following standard bracketing procedure. Two analyses of the R10 rutile standard (Luvizotto et al., 2009) were used as the primary rutile reference, and one analysis of the R19 rutile standard (489.5 ± 0.9 Ma, Zack et al., 2011) was used for quality control, followed by six analyses of the rutile grains. This sequence was repeated three times with an analysis of the R19 standard and two analyses of the R10 standard at the end of the session.

The data were corrected for U–Pb fractionation and for mass bias by repeated measurements of the R10 rutile standard. The R19 rutile standard measurements, treated as unknowns, were used to control the reproducibility and accuracy of the corrections. These standards yielded an age of 490 ± 3 Ma (MSWD = 1.11; n=13) during the April 2016 session and 493 ± 12 Ma (MSWD=2; n=12) during the December 2017 session. The data reduction was carried out with the data reduction

scheme, VizualAge_UcomPbine, a set of Iolite procedures that work with Igor Pro (Chew et al. 2014). All the data were plotted at 2 sigma on Tera-Wasserburg Concordia diagrams using the Isoplot 3.75 software (Ludwig, 2012).

Analyses of $^{40}Ar/^{39}Ar$ were performed at the University of Manitoba (Canada) using a multi-collector Thermo Fisher Scientific ARGUS VI mass spectrometer linked to a stainless steel Thermo Fisher Scientific extraction/purification line, a Photon Machines (55 W) Fusions 10.6 CO_2 laser, and a Photon Machines (Analyte Excite) 193 nm laser. Isotope abundances were corrected for extraction-line blanks, which were determined before every sample analysis. Line blanks in both the Excimer and CO_2 system averaged ~3 fA for mass 40 and ~0.013 fA for mass 36. Mass discrimination was monitored by online analysis of air pipettes based on a power law relationship (Renne et al., 2009), which gave D = 1.0081 ± 0.0002 per amu, based on 71 aliquots interspersed with the unknowns. A value of 295.5 was used for the atmospheric $^{40}Ar/^{36}Ar$ ratio (Steiger and Jäger, 1977) for the purpose of routine measurement of mass spectrometer discrimination using air aliquots, and correction for atmospheric argon in the $^{40}Ar/^{39}Ar$ age calculation. Corrections were made for neutron-induced ^{40}Ar from potassium, ^{39}Ar and ^{36}Ar from calcium, and ^{36}Ar from chlorine (Roddick, 1983; Renne et al., 1998; Renne and Norman, 2001). The data were plotted using DensityPlotter (Vermeesch, 2012). Complementary information is given in Appendix A2.

Results

Petrography of the tourmalinized wall rocks

Tourmaline is a common mineral in the wall rocks to the W-veins in the Panasqueira deposit, but may also be observed far from the deposit, bordering either barren quartz veins or even "dry" joints. The tourmaline-bearing rocks extend from the vein/joint boundaries for distances varying from a few cm (≤10) to 1 m, or roughly 25 cm on average.

As first noted by Bussink (1984), and later by Foxford et al. (1991), thin quartz veinlets (1-5 mm in average) are common in the tourmaline-bearing wall rocks adjacent to the main veins, and in many cases define the vein margins. They display clear evidence for a crack-seal mechanism of opening, and are labelled Qcs hereafter (Fig. 3-A).

There is a clear organization of the tourmaline in layers parallel to S_0, preserving the protolith fabric, as pointed out by Codeço et al. (2017). The tourmalinized wall rocks generally contain more than 50 vol.% tourmaline and tourmaline abundance is locally high enough to classify the rock as tourmalinite. Tourmaline is invariably associated with quartz, and with muscovite in the most pelitic protoliths, where the mica defines the schistosity. It is accompanied by abundant rutile (see

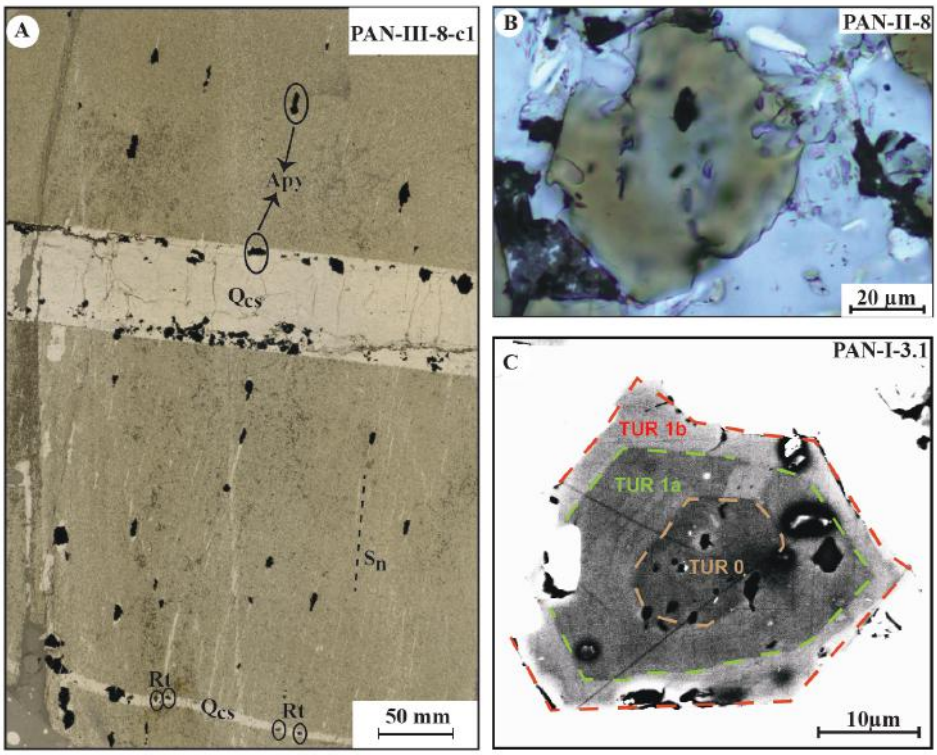

Figure 3. **A**. Typical tourmalinized wall-rock, with Qcs quartz veinlets. Sn, regional schistosity. Note the numerous overprinting arsenopyrite (Apy) crystals. Sample PAN-III-8-c1 (NL). **B**. Poorly zoned tourmaline 1 seen in natural light. Sample PAN-II-8. **C**. Typical zoning of tourmaline 1(BSE), showing the three Tur0, Tur1a and Tur1b zones. Sample PAN-I-3-1.

below), zircon and fluor-apatite and sporadic monazite or xenotime crystals, usually no more than 10-20 µm, and commonly only a few µm in diameter. Aggregates of micrometer-scale crystals of zircon and xenotime or zircon and monazite are common. In addition to these ubiquitous accessories to the tourmaline, a number of other hydrothermal minerals were later involved in the alteration of the Panasqueira wall rocks, and include quartz (silicification), topaz, muscovite, sulfides (pyrrhotite, sphalerite, chalcopyrite, arsenopyrite), apatite and siderite.

Tourmaline textures

Tourmaline habit and zoning: The tourmaline habit may be either acicular, with lengths between 500 µm and 1 mm and diameters of 20-50 µm, or, more commonly, stocky prismatic, with lengths between 50 and 150 µm and diameters of 10-20 µm (Fig. 4-A, B). The prisms are mostly sub-parallel to the schistosity of the Beira schists (Fig. 4-A), but they may be perpendicular to it. Contact metamorphic cordierite was replaced by tourmaline (Bloot and de Wolf, 1953).

The tourmaline crystals are brown and weakly zoned in thin section (Fig. 3-B), but display well-characterized growth zoning in SEM images (Fig.3-C and 4-C, D) expressed as nearly homogenous

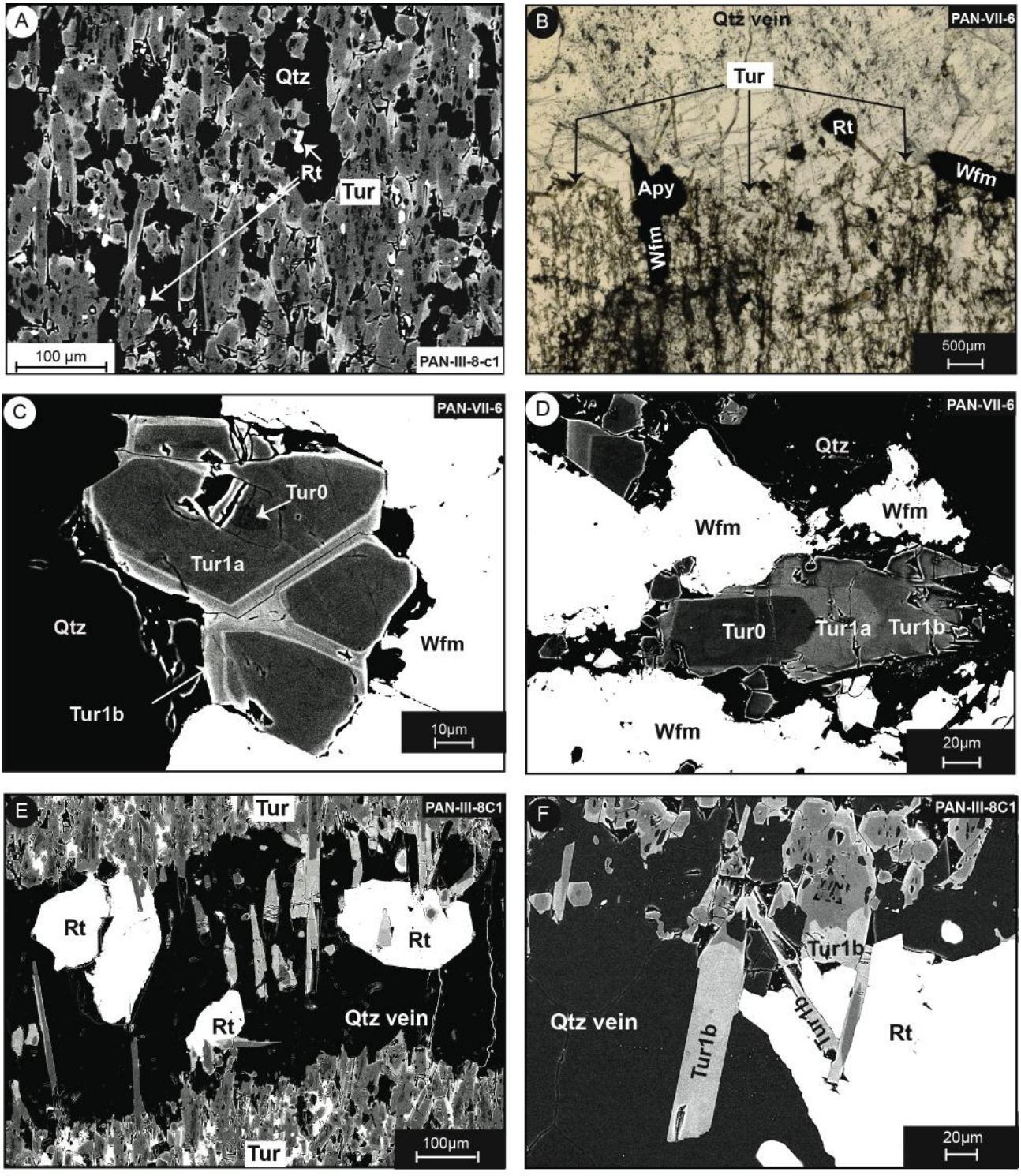

Figure 4. **A**. Typical early assemblage in the tourmalinized wall-rock, with Tur1 elongated along (erased) schistosity and disseminated rutile. Sample PAN-III-8-c1 (SEM). **B**. Acicular tourmaline in a silicified wall-rock. Sample PAN-VII-6-b1 (NL).). **C**-**D**. Evidence for coeval growth of Tur1b and early wolframite: **C**. Wolframite growth inhibited the development of Tur1b zones; **D**. Wolframite growth progressively inhibited first Tur1a, then Tur1b growth. Sample PAN-VII-6-b1 (SEM). **E**-**F**. Evidence for coeval growth of Tur1b and the W-rich rutile in a Qcs veinlet. Sample PAN-III-8-c1 (SEM).

zones of variable grey intensity, with sharp boundaries. A dark irregularly shaped core is commonly present, although not systematically, but there is no evidence for sector zoning. These cores are interpreted to be relicts of the early tourmaline and are labelled Tur0 hereafter. The outer parts of the tourmaline prisms comprise a medium grey zone, labelled Tur1a and a clearer rim, labelled Tur1b. In rare cases, there is an outermost rim characterized by the recurrence of a darker hue.

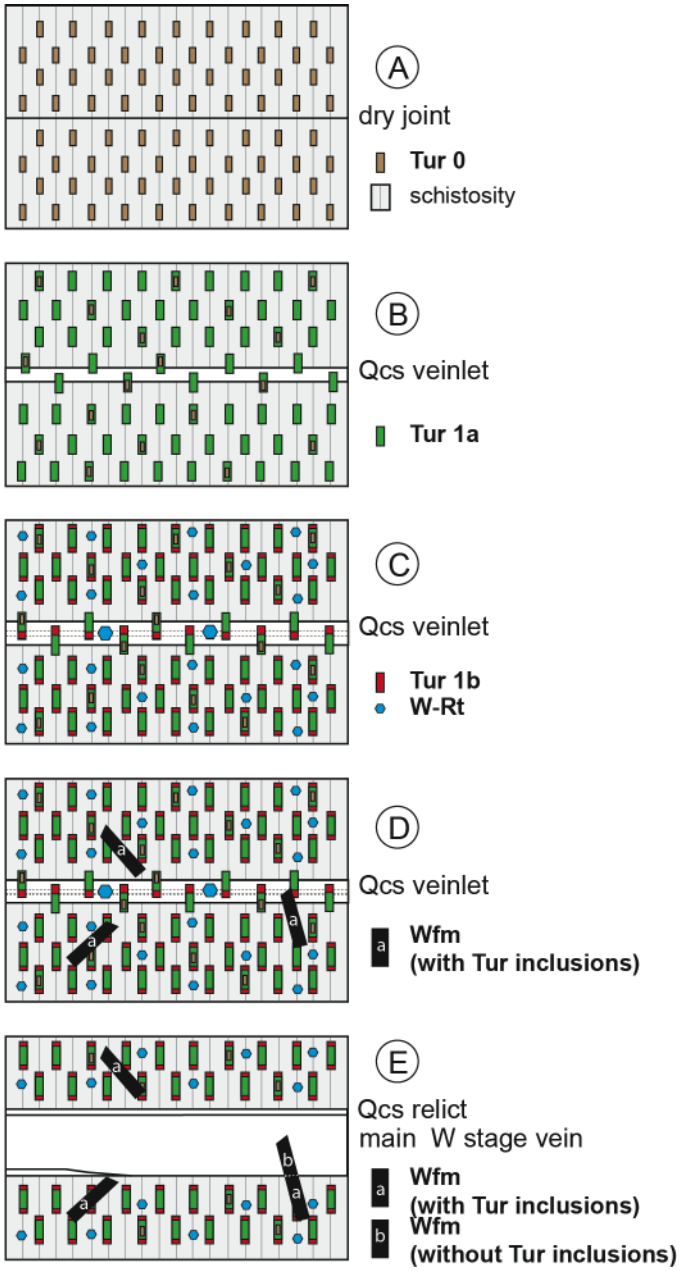

Figure 5. Synthesis of the stage Ia tourmalinization. **A**. Initialization of alteration (Tur0) in relation to simple "dry" joints. **B**. Main tourmaline development (Tur1a) and first increments of opening in Qcs veinlets. **C**. Growth of Tur1b tourmaline relative to increments of Qcs opening and coeval rutile growth. **D**. Local variant with early wolframite growing in the wall-rock coevally with Tur1b. **E**. Transition to the main wolframite deposition stage

Some changes in the relative proportions of the different zones may be observed in relation to the distance from the vein boundaries. Distal to veins, the proportion of Tur0 zones is higher, on

304 average these zones are wider, locally the crystals display regular (prismatic) shapes and the
305 development of Tur1b rims is less pronounced. Furthest from the veins, the Tur1b rim may even be
306 absent. Close to the veins, there is a greater development of the Tur1b zone, and the Tur0 cores are
307 less common, corroded, and tend to represent a comparatively smaller proportion of the crystal
308 volume. On the basis of a limited number of examples, it would appear that this tendency is roughly
309 correlated with the presence of abundant wolframite in the nearby vein. Indeed, in the wall rocks of
310 barren quartz veins, either in outcrop, or in the deeper levels of the mine (L3), Tur1b is usually
311 absent.
312 Micro-inclusions are common in the tourmaline, although not systematically distributed. In order
313 of importance, they are: zircon, rutile, quartz, and rare monazite, pyrite, and apatite. Most
314 commonly, the inclusions "overprint" the zone boundaries, and in most cases, the proportion of
315 inclusions is the same in the Tur1a or Tur1b zones. The Tur0 cores are relatively free of inclusions,
316 except for those of quartz. The zircon may be zoned in respect to their U-Th content. In addition,
317 microanalysis revealed the probable presence of concealed micro-inclusions (see below).
318 *Tourmaline and Qcs quartz veinlets:* Tourmaline prisms are systematically present at the walls
319 of the Qcs veinlets, displaying both Tur1a and Tur1b zones, the latter usually developed to a far
320 higher extent than in the wall rocks (Fig.4-E, F). Thus, as pointed out by Foxford et al. (1991), the
321 development of both the main Tur1a tourmaline prisms and the Tur1b rims was coeval with the first
322 increments of vein opening evident by the Qcs veinlets. This is pictured schematically in Fig. 5. The
323 very existence of Tur0, which is typically absent from the Qcs veinlets, nonetheless demonstrates
324 that the onset of tourmalinization was earlier than these veinlets (stage A in Fig. 5).
325 *Tourmaline and other alteration minerals:* Irrespective of the nature and the number of
326 hydrothermal minerals in the wall rocks, the tourmaline crystals invariably display the same
327 sequence of Tur0-Tur1a-Tur1b crystallization. Other alteration minerals are typically later. For
328 example, the occurrence of topaz and/or muscovite is accompanied by a distinct overgrowth on
329 Tur1b rims. In the same way, the development of apatite-bearing vugs in the tourmalinized wall
330 rocks was accompanied by distinct overgrowths on the undissolved tourmaline crystals. As sulfides
331 (chalcopyrite, sphalerite, pyrrhotite) and siderite are mainly present as stringers in the wall rocks, it
332 is easy to recognize that these stringers overprint tourmaline 1 prisms and their characteristic
333 zoning.
334 Small euhedral arsenopyrite crystals, a few 100 μm in diameter, are frequently disseminated in
335 the wall rocks (Fig. 3-A), locally (but not commonly) with inclusions of zoned tourmaline prisms.
336 Nevertheless, arsenopyrite grew after the Tur0-Tur1a-Tur1b sequence, because: (i) arsenopyrite
337 mostly replaced tourmaline prisms, and (ii) arsenopyrite overprinted Qcs veinlets (Fig. 3-A).

Tourmaline and wolframite: Wolframite from the mineralized veins is not, as a rule, associated with tourmaline but developed as large crystals along the walls of the open fractures. There are rare occurrences of the development of wolframite crystals in the wall rock, close to the mineralized veins (Fig. 4-B). These crystals include zoned tourmaline, and detailed observations show that wolframite growth was either coeval with Tur1b rim development or slightly later (Fig.4-C, D). This wolframite was, in turn, reworked in relation to the main opening and deposition of the main wolframite, which is consistently devoid of any tourmaline inclusions (stages E and F in Fig. 5).

Rutile textures

Rutile is systematically associated with tourmaline, being present both in the wall rocks, as small (from 10 µm to 80-100 µm) crystals, scattered or densely disseminated, or as large (up to 500 µm or more) isolated crystals in the Qcs veinlets, where they were clearly coeval with Tur1b growth (Fig. 4-E, F). Micro- to nano-inclusions (from about 1 µm, to <100 nm) of wolframite are common. They are usually located at crystallographic boundaries (e.g., faces intersections, twin planes, quartz inclusion boundaries) showing that they were coeval with the host rutile (Fig. 6-A). Their compositions, estimated from SEM-EDS measurements, are ferberitic, with Fe/Fe+Mn ratios between 0.67 and 0.83.

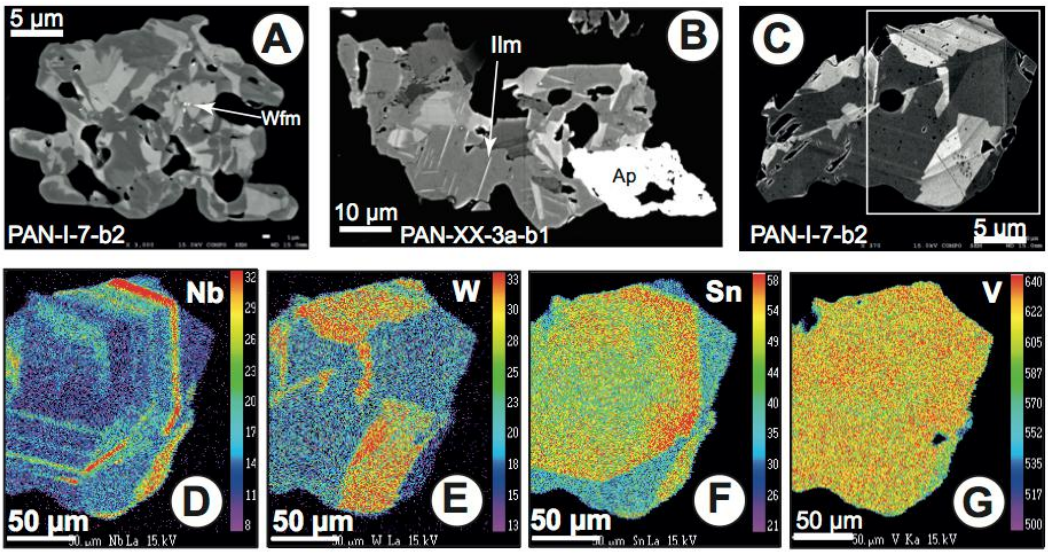

Figure 6. Panasqueira rutile. A, B, C: Back-scattered SEM images. of Panasqueira rutile. **A**. Crystal aggregate from the wall-rock of a wolframite-bearing vein. Note the primary wolframite nano-inclusions (Wfm). **B**. Crystal in the wall rock of a barren vein from the deep L3 level. Note the ilmenite lamellae (Ilm) and the late apatite (Ap), overprinting the rutile crystal. **C**. Large isometric crystal from a Qcs vein in the wall-rock of a wolframite-bearing vein. Note the superimposition of sector zoning (SZ) on the compositional (oscillatory) zoning. Square: location of images D to G. **D to G**: false-color X-ray (EPMA) images, showing the differential effect of SZ on the minor element concentrations, and the anti-correlation of W and Nb in the OZ.

In the barren wall rocks, rutile crystals are less abundant and are characterized by the presence of inclusions of ilmenite lamellae (Fig. 6-B).

Tourmaline chemical composition

Major element crystal chemistry: For reasons made explicit in Appendix A0, most analyses were performed using SEM-EDS. A total of 86 crystals from 19 representative samples was analyzed (Appendix A3: Table A3). No systematic variation in the compositions of the different zones was evident, however, either as a function of the distance to the vein boundary, or among tourmaline crystals from different settings (wall rock, Qcs veinlet, inclusions in early wolframite).

The structural formulae were calculated by normalizing to 26.5 (O, OH, F), which (with the assumption of stoichiometric boron) allowed us to take into consideration the fluorine content and not assume the filling of the Y site, which may contain Li, and possibly vacancies (Bosi, 2018). The generalized structural formula of the tourmaline super-group is $XY_3Z_6(T_6O_{18})(BO_3)_3V_3W$ (Bosi, 2018). The T site is occupied primarily by Si, which may be replaced by minor Ti, Al or B. The nine-coordinated site X may be occupied by Na^+ and Ca^{2+}, or minor K^+, and vacancies ($^X\square$) may be present. This defines the main chemical groups of tourmaline: alkali, calcic and alkali-deficient groups (Henry et al. 2011). The V, or (O)3, site is occupied mainly by OH (and possibly O), whereas the W, or (O)1, site is occupied by OH, F or O, defining the hydroxy, fluor, and oxy groups, depending on the dominant anion in the site. The six-coordinated Z site is mainly occupied by trivalent cations (mainly, Al^{3+}, but also Fe^{3+}, Cr^{3+}), but may contain divalent cations, mainly Mg (Bosi, 2018). The six-coordinated Y site is occupied by mono- (Li^+), bi- (Mg^{2+}, Fe^{2+}, Mn^{2+}) and tri-valent (mainly Al^{3+}, and possibly Fe^{3+}, Cr^{3+}) cations, but vacancies ($^Y\square$) may also be present (Bosi, 2018). Following the criteria of Henry and Dutrow (2011), calculated tourmaline formula were rejected if Si was > 6.15 atoms per formula unit (*apfu*), the sum of the Y + Z + T cations was >15.5 *apfu*, or the sum of the X-site cations exceeded 1.1 *apfu*. For reasons given in Appendix A0, all analyses yielding Si *apfu* values > 6.12 were rejected. Using the empirical formula of Bosi (2018), the ^{Z}Al *apfu* content of the Z site was found to be relatively constant, ~5.23 apfu, irrespective of the zone, and, whereas there was sufficient Mg to fill this site in Tur0 and Tur1a, a small complementary content of ^{Z}Fe was necessary in Tur1b (Table A3, Appendix A3).

Based on the classification diagram of Henry et al. (2011), which compares the normalized X-vacancy to the Mg# (Mg/Mg+Fe) ratio, the tourmaline classifies mainly as schorl (Fig. 7-A). There is a systematic shift from Mg-rich (ferro-dravite) to Fe-rich compositions for the sequence Tur0 to Tur1a to Tur1b, and a tendency towards foitite compositions. Indeed, as shown in Figure 7-B, the X-site vacancy is between ~0.2 and ~0.6 *pfu* (and thus, the Panasqueira tourmaline trends toward

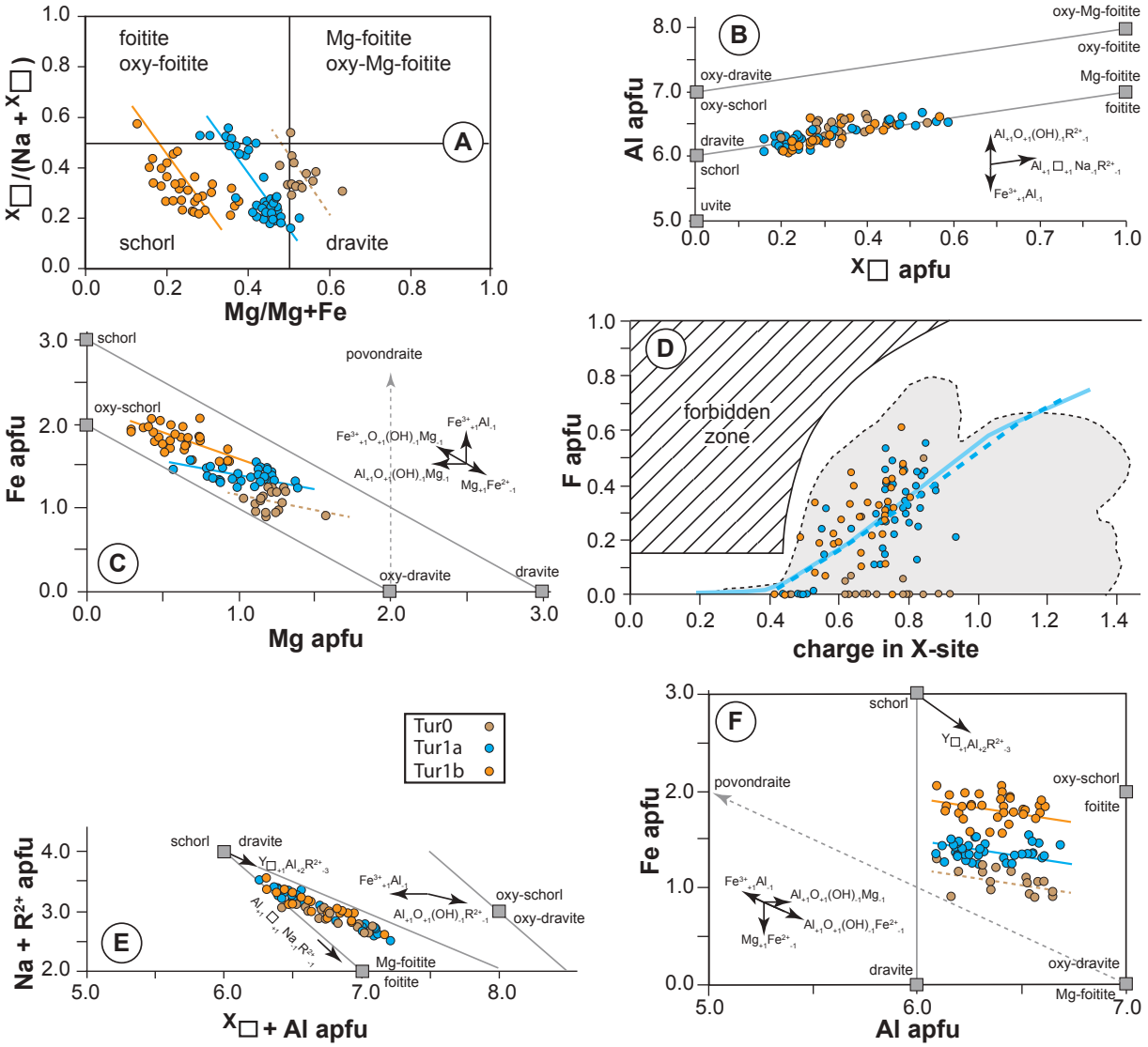

Figure 7. Crystal chemistry of the Panasqueira tourmaline, illustrating the characteristics of the Tur0, Tur1a and Tur1b zones. Note in all the diagrams the continuity of composition variations among the three zones. **A**. Classification diagram. **B.** Al vs. X-site lacune diagram, demonstrating the presence of a foitite component. **C**. Fe vs. Mg diagram, illustrating the presence of an oxy-schorl component, together with the classical schorl-dravite exchange vector. **D**. Linear relationships between F and the X-site charge; the forbidden zone and references are from Henry and Dutrow (2011): grey domain, worldwide tourmaline (~ 8,900 values); light blue line: Cruzeiro gold mine fibrous tourmaline; dashed blue line: McCombe pegmatite tourmaline (magmatic trend). **E**. Na + R2+ vs. Al+X-site lacune diagram, illustrating the deviation from the schorl (dravite)-foitite (Mg-foitite) exchange line due to a combination of the oxy-schorl (dravite) exchange vector and a vector responsible for the creation of Y-site vacancy. **F**. Fe vs. Al diagram, showing the combination of all exchange vectors involved in the Panasqueira tourmaline.

alkali-deficient species) corresponding to the operation of the $Al_{+1}{}^{X}\square_{+1}Na_{-1}R^{2+}{}_{-1}$ vector, which leads to a solid solution between schorl-dravite and foitite-Mg-foitite. From Figure 7-C, E and G, it is evident that other vectors combined to displace the observed trends from the preceding trend. The $Al_{+1}O_{+1}(OH)_{-1}(Mg, Fe)_{-1}$ vector seems to have been particularly important, implying an oxy-schorl

(or oxy-dravite) component, but the intervention of another exchange vector $^{Y}\square_{+1}Al_{+2}R^{2+}_{-3}$, responsible for an Y-site vacancy (Bosi, 2011), seems to have been equally important. Indeed, a Y-site vacancy is observed in our analyses, commonly larger than 0.1 *apfu*, and also those of Codeço et al. (2017) and Launay et al. (2018) (Table 3, Appendix 3). This vacancy cannot be due to ignored Li, because the LA-ICP-MS results (see below) show that the Li content is negligible, being at most of ~330 ppm and averaging ~170 ppm (Tur1a) or ~290 ppm (Tur 1b); these contents would be reflected by an amount of no more than 0.05 *apfu* Li and more commonly 0.02-0.04 *apfu*.

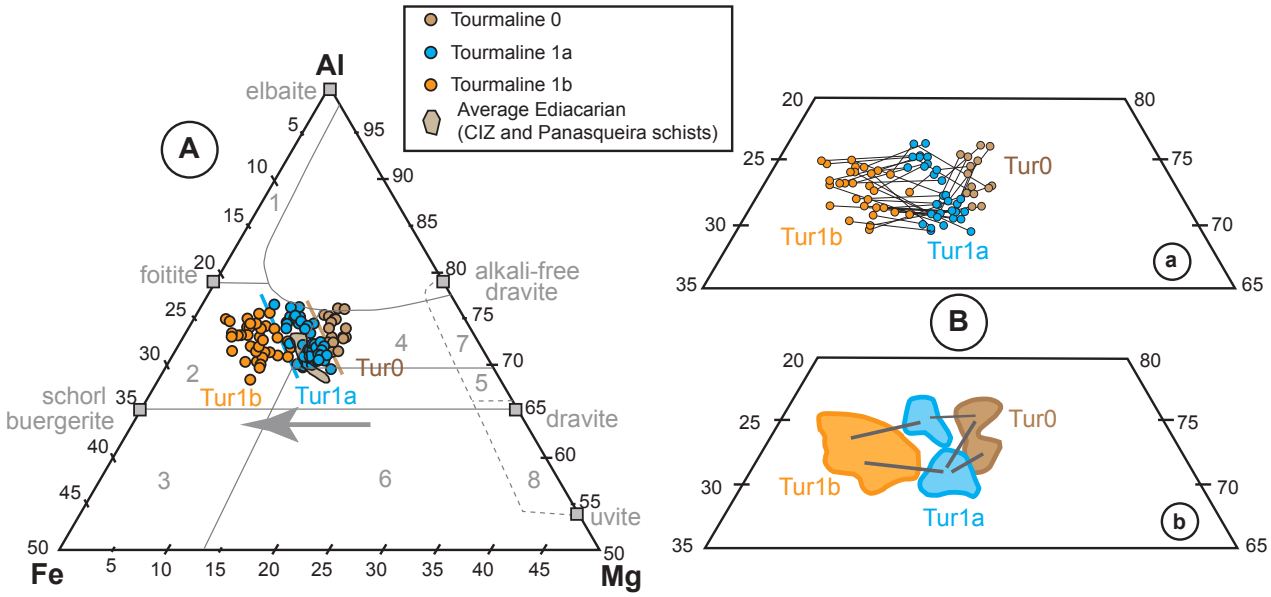

Figure 8. **A**. AFM diagram for the Panasqueira tourmaline, with location of the main tourmaline end-members. (1)-(8) reference fields from Henry and Guidotti (1985): (l) Li-rich granitoids, (2) Li-poor granitoids, (3) Fe^{3+}-rich quartz-tourmaline rocks (hydrothermally altered granites), (4) Al-buffered metapelites, (5) not Al-buffered metapelites, (6) Fe^{3+}-rich quartz-tourmaline rocks, calc-silicate rocks, and metapelites, (7) low-Ca meta-ultramafics and Cr,V-rich metasediments, and (8) metacarbonates and meta-pyroxenites. Compositions of CIZ schists from Oosterom et al. (1984) and De Amorin (2017). The grey arrow emphasizes the global increase in Fe/Fe+Mg ratio from Tur0 to Tur1b. **B**. Enlargement of A, illustrating the sequence Tur0-Tur1a-Tur1b: (a) individual paths, (b) synthesis. Note that, if there is a jump from a zone to another, the starting and final compositions differ for each individual crystal.

In contrast to Tur0, which appears to be essentially free of fluorine, there is a distinct and similar fluorine enrichment (up to ~1% F) of Tur1a and Tur1B, and a trend of increasing F *apfu* with X-site charge (Fig.7-D). The latter is due to the high X-site Na content; Tur1a and Tur1b are Ca-poor, whereas Tur0 is enriched in Ca, which, in turn, explains the higher X-site charge of Tur0 in Figure 7-D.

The complex covariations between aluminum, iron and magnesium that are depicted in Figure 7 are conveniently summarized in the AFM diagram of Figure 8-A, in which it is also possible to identify the most common compositional paths from Tur0 to Tur1a and then Tur1b at the crystal

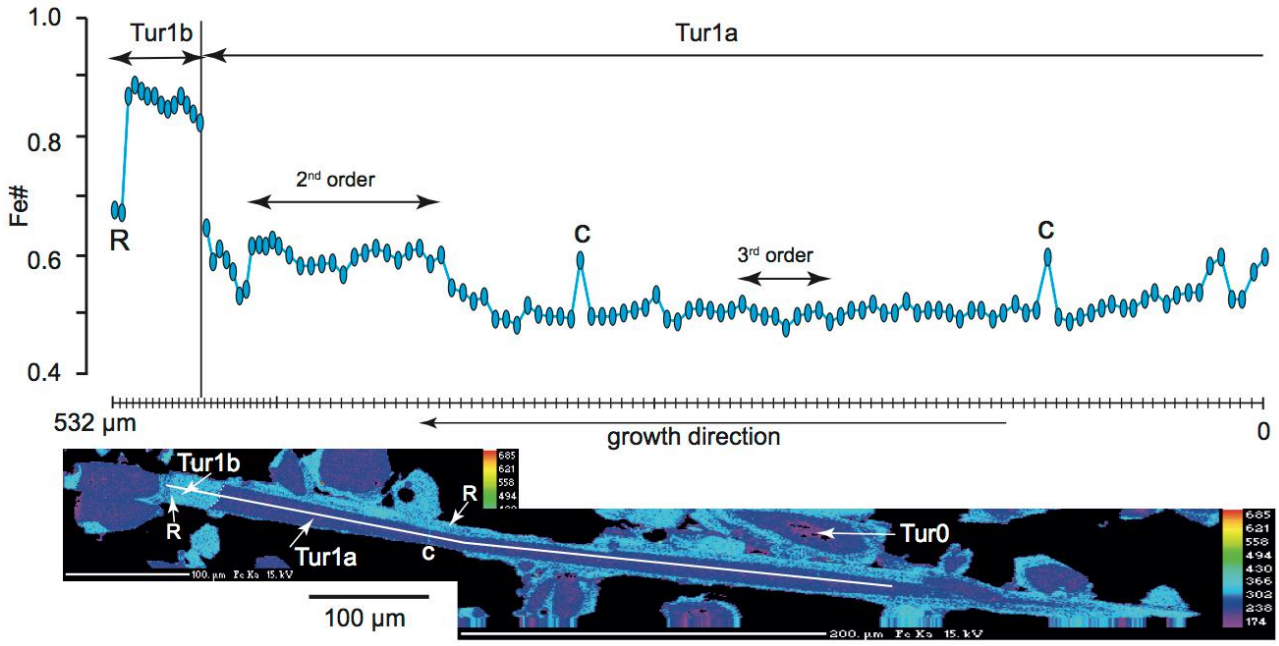

Figure 9. Profile of the Fe# ratio (Fe/Fe+Mg) along an acicular prism of tourmaline 1 (EPMA analyses), compared to the false color X-image of the same crystal (sample PAN-VII-6-b2). The height of the elliptical symbol corresponds to the estimated error on Fe#. Of the three zones (Tur0, Tur1a, Tur1b) seen on the X-image, only the two latter are documented in the profile. At the rim of Tur1b zone, a recurrence of low Fe# is observed ®. Note the second and third order modulations of the Fe# ratio along the profile. c: microcrack filled by Tur1b.

scale (Fig. 8-B). This figure illustrates an apparently continuous variation of the Fe to Fe+Mg ratio (Fe#) from Tur0 to Tur1b, although detailed profiles show that there were small-scale modulations of the Fe# during crystal growth (Fig. 9).

Trace element contents: As LA-ICP-MS analyses produce laser pits with a diameter of at least 24 µm, analysis to the desired detection limits was possible only for the largest Tur1 zones in a limited number of crystals. Moreover, the tourmaline cores (Tur0) were too small for them to be reliably analyzed, so analyses were restricted to the two external rims, Tur1a and Tur1b. A total of 77 spots, in 47 crystals from 7 samples were analyzed for their trace element concentrations. The REE concentrations were also analyzed, but to obtain the required signal, a laser beam diameter of 120 µm was necessary, and therefore only two crystals, from two samples, could be analyzed for the REE. This yielded an average composition of Tur1a and Tur1b zones from the two crystals. The results are summarized in Table 1 and detailed in Appendix A4 (Table A4).

For some elements, several LA-ICP-MS spectra displayed anomalous peaks (anomalous values in Table A4), interpreted as recording the presence of concealed micro- to nano-inclusions. Thus, a Mn outlier at 2,600 ppm was likely due to siderite, and a Zn outlier at 8,500 ppm is interpreted to be due to sphalerite. Several W anomalies record the presence of W-bearing minerals: W-bearing rutile, where correlated with both Ti and Nb-Ta-Sn anomalies; cuprotungstite, where correlated

	Tur1a			Tur1b			detectio
	min	**max**	**average**	**min**	**max**	**average**	level
Li	26	170	72	48	288	130	
Be	1	21	8	0,8	21	4	
Sc	5	32	17	7	26	12	2
Ti	530	4360	1753	849	2840	1714	
V	37	613	341	11	742	282	
Cr	4	1027	271	9	601	156	8
Mn	135	528	421	310	606	468	20
Co	*0.2*	13	2	*0.2*	3	1	0.3
Ni	3	56	16	*0.2*	23	7	0.3
Cu	*0.3*	12	2	*0.3*	23	1	0.5
Zn	237	856	631	161	925	656	
Sr	10	285	79	7	131	40	
Y	*0.2*	7	1.4	*0.2*	5	0.9	0.3
Nb	*0.2*	12	0.6	*0.2*	2	0.2	0.3
Ta	*0.2*	0.5	0.2	*0.2*	0.2	0.2	0.3
Sn	4	54	24	4	157	19	3
W	*0.2*	29	4	*0.2*	21	3	0.4
Pb	2	33	6	1	15	4	

Table 1. Summary of LA-ICP-MS trace element analyses for the Panasqueira tourmalines. All contents in ppm. For the purpose of average calculations, the bdl (below detection level) in Table A4 were taken at half the detection level values (i.e., the without bias best estimates) when needed (italics). As a result, the averages for Nb (0.2 ppm) and Ta (0.2 ppm) are not provided in the table.

with a Cu anomaly (a rare occurrence); and wolframite, where no correlation was observed with either Ti or Cu. Most of these W anomalies were found in the Tur1b zones.

The results of the trace element analyses are illustrated in Figure 10-A (trace elements except REE) and Figure 11 (REE profiles). As seen in Figure 10-A, Ti, (530 to 4,360 ppm), Zn (160 to 930 ppm) and Mn (135 to 600 ppm) are the most abundant trace elements, followed by Li (40 to 330 ppm), V (10 to 740 ppm) and Cr (10 to 1,000 ppm). Strontium (7 to 285 ppm) and Sn (4 to 160 ppm), are present in lower concentrations, followed by Sc (5 to 30 ppm), Be (3 to 20 ppm), and Pb (1 to 18 ppm). Concentrations of other elements were commonly below the detection level (*bdl*), e.g., Ni (up to 56 ppm), Co (up to 13 ppm) and Y (up to 7 ppm). Most measured tungsten concentrations were between 0.4 and 30 ppm, but for ~25 % of analyses of Tur1a and 50 % of Tur1b, the W concentration was below the detection level of 0.4 ppm. The measured concentrations for Nb are between 0.1 and 3.2 ppm, but for ~ 75% of the analyses, they were below the detection level of 0.3 ppm; the few measured Ta values were between 0.3 and 1.6 ppm; the overwhelming majority of analyses yielded values below the detection level of 0.3 ppm. From the limited REE data, the ∑REE concentration is low (between 1.2 and 12 ppm), and the REE profiles are

characterized by high La_N to Yb_N ratios of 6.37 to 6.77, and slightly negative Eu_N/Eu^*_N anomalies (0.65 to 0.83) (Fig. 11).

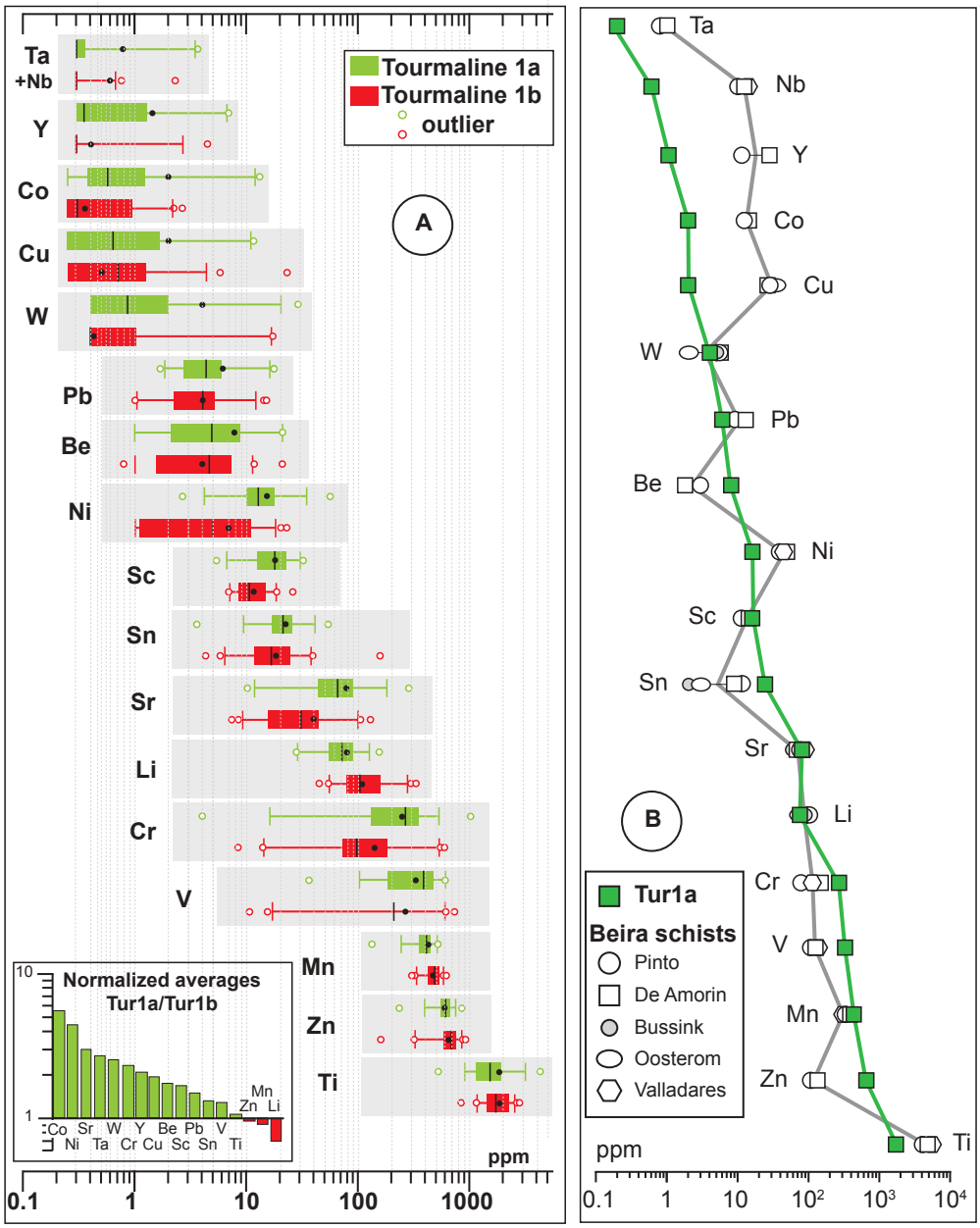

Figure 10. Trace-element patterns in Panasqueira tourmaline 1. **A**. Box plots of LA-ICP-MS results for tourmaline 1a and 1b. The full box represents the lower quartile to upper quartile interval. The whiskers represent the 5%-95% interval. Black circle: average value, black vertical line: median value. Open circle: outlier value, comprised in the 5% lowest or highest data. Inset: normalization of average values of Tur1a to the Tur1b reference. **B**. Comparison of trace-element distribution (average values) between Panasqueira tourmaline 1a and Beira schists. The elements are arranged from left to right in accordance with their increasing concentration in tourmaline 1a. Data for Beira schists are from De Amorin (2017), Bussink (1984), Oosterom et al. (1984), Pinto (2014) and Valladares et al. (2002).

From Figure 10-A, it can be seen that Tur1a and Tur1b compositions are quite similar, although there are minor but significant differences between them with most of the trace elements being

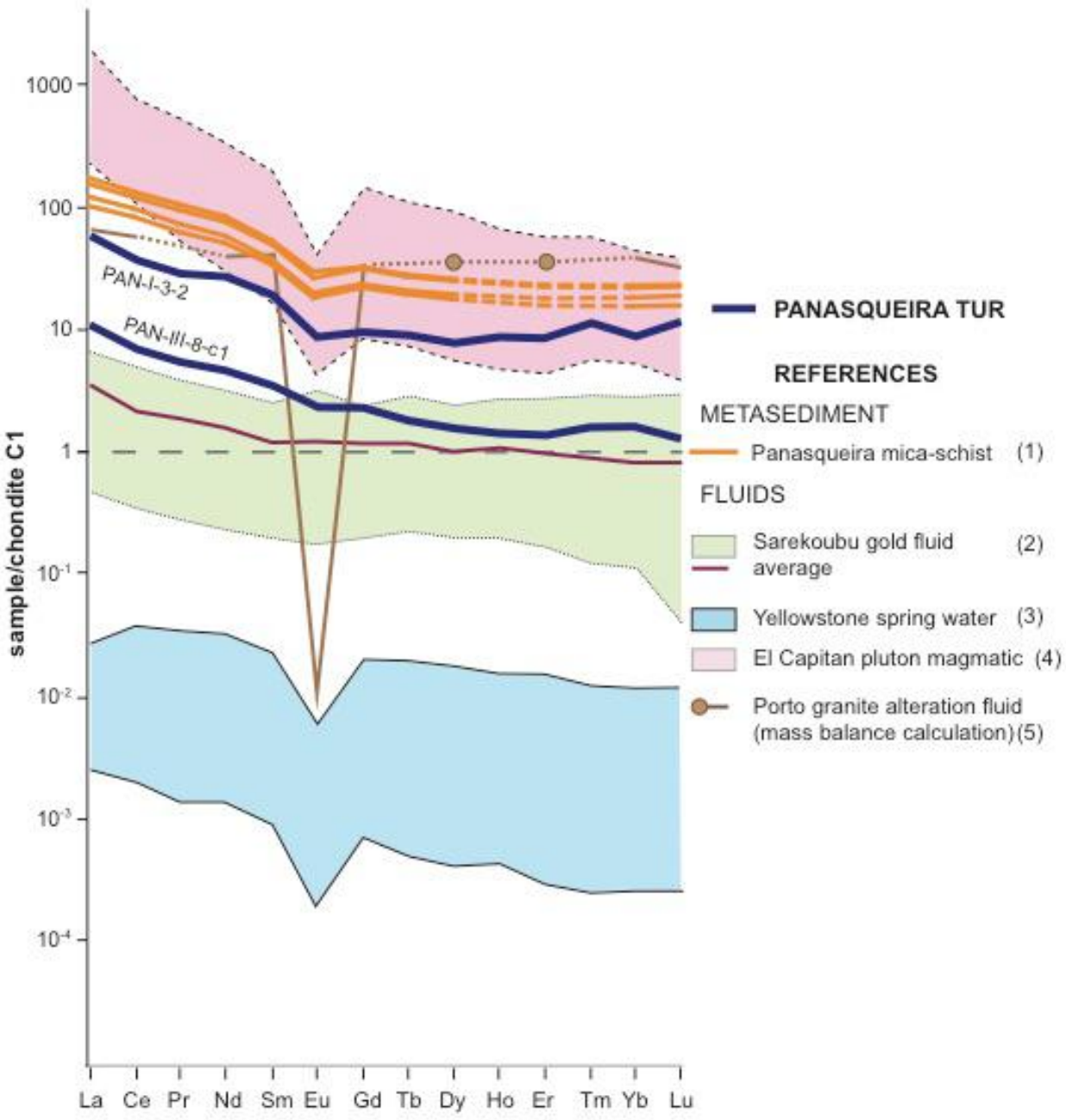

Figure 11. Chondrite-normalized REE profile for the Panasqueira tourmaline (samples PAN-I-3-c2 and PAN-III-8-c1) compared to the profiles for the Panasqueira metasediments (1: De Amorin, 2017), the fluids associated to the Sarekoubu orogenic gold deposit (2: Xu et al., 2008), the Yellowstone spring water (3: Lewis et al., 1997) and magmatic-derived fluids (4: Banks et al.,1994; 5: Poitrasson et al.,1995) (explanations in the text).

depleted in Tur1b relative to Tur1a. The notable exceptions to this are Li, Mn and Zn, which are depleted in Tur 1a. This is also evident from the differences in the average values (Table 1, and insert in Figure 10-A), and from the shift between the full boxes (lower quartile to upper quartile interval) in the box plot of Figure 10-A.

A principal component analysis was performed on the trace element data (using the JM Pro software), the results of which are presented in Figure 12. Three axes (PC1-3) explain 52.7 % of the

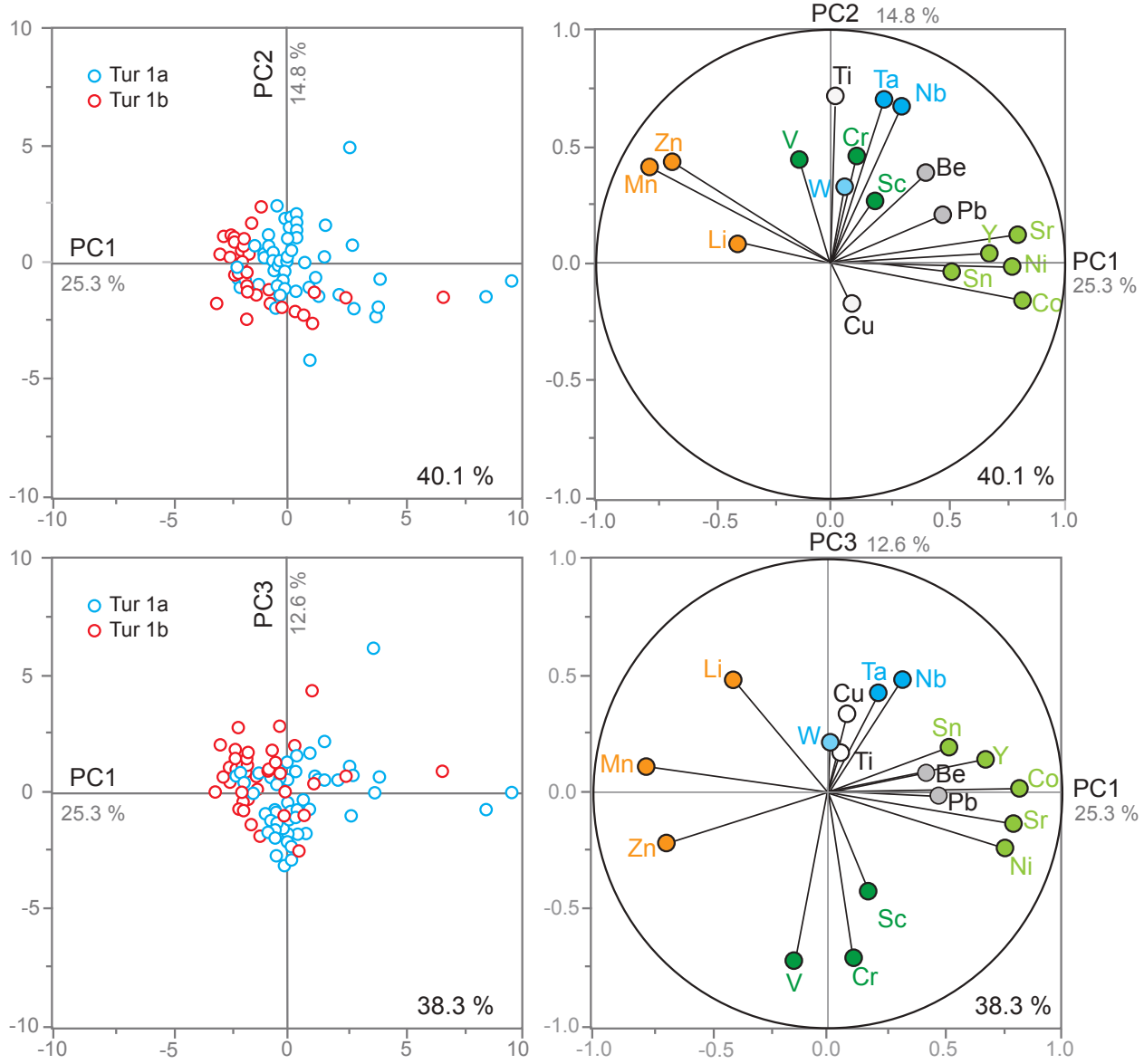

Figure 12. PCA analysis of the trace element composition of the Panasqueira tourmaline, allowing the definition of several groups of trace elements, namely: Mn-Zn-Li, Cr-V-Sc, Co-Ni-Sr-Y-Sn, Be-Pb, and Nb-Ta (explanations in the text).

variance. The first axis (PC1) clearly distinguishes Tur 1a and 1b, as well as two groups of elements: a group A (Li-Mn-Zn) and a group B (nearly all other elements) reproduce, as expected, the relationship observed in Figure 10. The PC2 and PC3 axes display correlations within group B, providing evidence of several subgroups, namely: Co-Ni-Sr-Y-Sn, Cr-V-Sc, Nb-Ta and Pb-Be. Copper, Ti, and W behave independently, and W appears uncorrelated to Nb-Ta.

In binary plots, elements of group A display rough linear trends expressing positive correlations (when outliers are excluded), as seen for example in Figures 13-A to C, and predicted by the principal component analysis. Similarly, elements of group A display negative correlations with elements of group B, as seen, for example, in Figures 13-D to H. Less expected were the linear

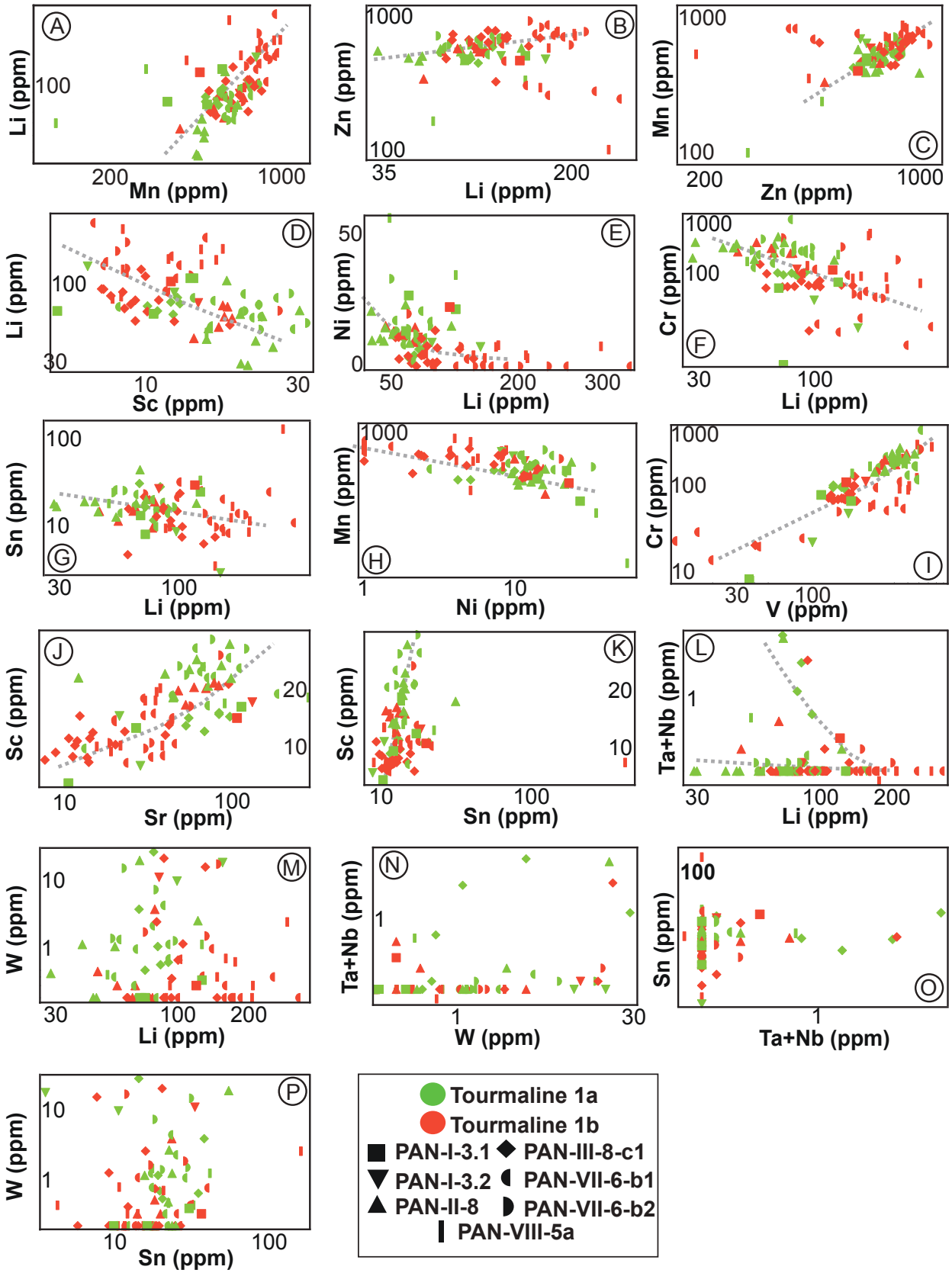

Figure 13. Binary plots of selected trace elements from Panasqueira tourmaline, showing contrasting behaviour, including positive, negative and null correlations, depending on the elements (explanation in the text).

relationships between elements from the various B subgroups, as seen for example in Figures 13-I to K. The rare metals (W, Nb, Ta) behave differently. Whereas Nb-Ta show a very loose negative correlation with Li (Fig.13-L), there is no correlation between W and Li (Fig. 13-M), nor between W and Nb-Ta (Fig. 13-N). Finally, Sn is not correlated with Nb-Ta (Fig. 13-O) or with W (Fig. 13-P).

Rutile composition:

The composition and zoning of the Panasqueira rutile have been described in detail in Carocci et al. (2019) and only a summary is given here. This rutile contains variable proportions of: Fe from 0.18 to 2.95 wt%, V from <1000 ppm to 3.48 wt%, Cr from <1000 ppm to 2.41 wt%, Nb from <1000 ppm to 1.64 wt%, Ta from <1000 ppm to 2.17 wt%, and W from 0.20 to 10.7 wt%. Despite locally high values, Nb and Ta concentrations are usually low; the Nb+Ta content is usually < 0.5 wt% and the Nb/Nb+Ta ratio varies from 0.05 to 0.97 (on average 0.6).

The crystals display marked sector zoning, exhibited mostly by W and Fe and, to a lesser extent, by Nb and Ta; Sn, V (and Cr), and display less evidence of zoning (Fig. 6- C to G). The maximum W concentration varies from 1.12 to 10.7 wt.% in the metal-rich sectors, depending on the sample; W concentrations in the metal-poor sectors vary between 0.26 to 1.40 wt %. As metal-rich sectors reach their highest W contents in wall rocks adjacent to veins in which wolframite is abundant, whereas in barren wall rocks the metal-rich sectors are less endowed in W (no more than 3.5 wt% W), it would appear that the W enrichment in rutile is related to the wolframite endowment in the nearby veins. Association of a very W-rich rutile with wolframite was also observed in the Puy-les-Vignes breccia-pipe tungsten deposit in the French Massif Central (Harlaux, 2016).

The sector zoning is superimposed on a conspicuous compositional zoning, expressed from the crystal scale down to the 10 μm to μm scale of the doublets characteristic of oscillatory zoning (Fig. 6-C). The zoning, however, is qualitatively and quantitatively the same irrespective of the rutile setting. All the minor elements, W, Nb(Ta), Fe, V, Cr and Sn, are involved in the compositional zoning. At all scales, W and Nb(Ta) are inversely-correlated, whereas Sn and V display inconsistent behavior, being either correlated with Nb(Ta) and inversely-correlated with W or the opposite.

The bulk evolution during crystal growth was variable from one crystal to the next, even at the sample scale. In some crystals, there is continuous evolution from a Nb-rich and W-poor core to a Nb-poor and W-rich rim, whereas the opposite is observed in others. Most commonly, however, the zoning displays moderate deviations from the average W content.

Age determinations

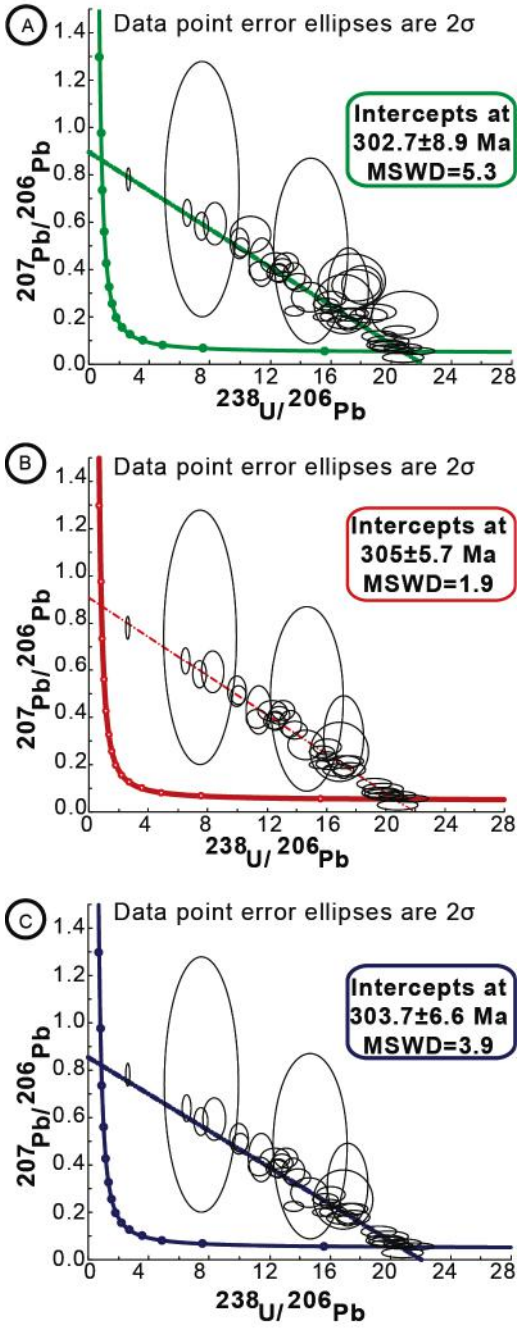

Figure 14. Results of U-Pb age determinations of wall-rock Panasqueira rutile (Tera-Wasserburg Concordia diagrams). Note the highly discordant behaviour of the rutile. **A**. All data, showing the importance of lead loss in the rutile crystals. **B**. Data remaining after elimination of analyses more affected by lead loss. **C**. Idem, with data constrained to be consistent with the common lead value of Stacey and Kramers (1975) at c. 300 Ma. Explanations in the text.

Rutile: Petrographic examination suggests that rutile from both the tourmalinized wall rocks and the Qcs veinlets were coeval with the early tourmaline and the earliest wolframite deposition. Unfortunately, the number of rutile crystals suitable for U-Pb dating was limited by the size of the laser spot (45 μm). Some crystals from Qcs crack-seal veins are large enough to be analyzed, but

very few crystals in the wall rocks reach 50 μm in diameter. Thus, only 22 crystals from 5 samples could be analyzed for their U-Pb isotopic compositions.

The analyzed crystals have variable concentrations of common lead, and low radiogenic Pb contents (Appendix 6, Table A6). On a Tera-Wasserburg diagram they plot in a discordant to a very discordant position, except for one sample (PAN-III-8-c1), which plots close to the Concordia curve. Figure 14 illustrates three regression lines: (i) using all the data, the regression line results in a discordia with a lower intercept at 302.7 ±8.9 Ma (2σ, MSWD =5.3) (Fig. 14-A), the poor quality of this age determination being due to large lead losses, (ii) a discordia in which data corresponding to the greater lead losses were ignored (Fig. 14-B), passes through the concordant data and yields a lower intercept at 305.2 ± 5.7 Ma (2σ, MSWD = 1.9), the upper intercept yielding a common lead $^{207}Pb/^{206}Pb$ ratio of 0.906, which is slightly higher than the 0.855 value predicted by the Stacey and Kramers (1975) model for the same age; and (iii) a discordia, anchored to the Stacey and Kramers composition at 305 Ma, yielding a lower intercept at 303.7 ± 6.6 Ma (2σ, MSWD = 3.9) (Fig. 14-C). A similar date of 303.7 ± 6.6 Ma, with a slightly higher MSWD value of 3.9 is obtained by constraining the regression to fit the Stacey and Kramers (1975) common lead composition,. A critical issue is the $^{207}Pb/^{206}Pb$ value of the common lead in the CIZ at c 305 Ma. At c. 320 Ma, the $^{207}Pb/^{206}Pb$ ratio of the Ediacaran and Tremadocian metasediments was between 0.885 and 0.96 (calculated from Nägler et al. 1993, 1995 data). It thus evident that the 0.906 value for the common lead in the Panasqueira rutile is in accordance with the regional values, and, consequently, the date of 305.2 ± 5.7 Ma is interpreted as the best estimate for the crystallization age of the rutile. As Polya et al. (2000) demonstrated that the Qcs veins immediately preceded the main opening of the quartz vein system and wolframite deposition, the age of c. 305 Ma is also interpreted to be the age of the main wolframite deposition.

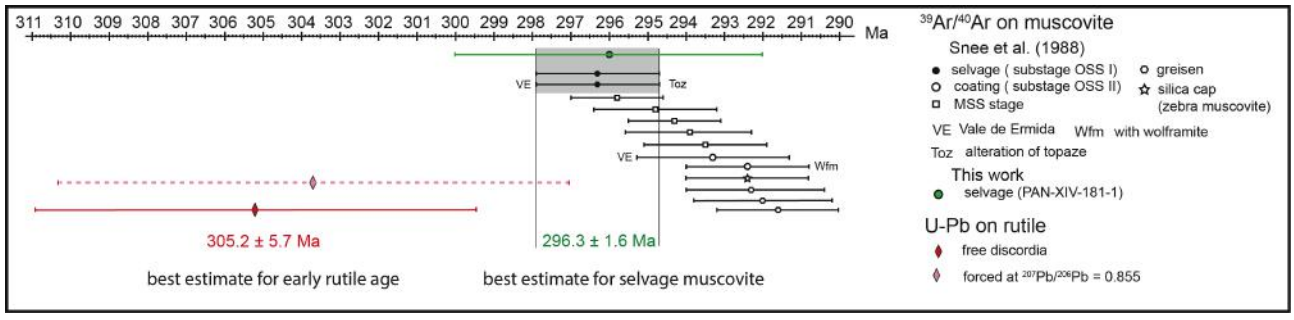

Figure 15. Synthesis of radiometric ages for the Panasqueira deposit, comparing results of the present work with those of Snee et al. (1988). Explanation in the text.

Complementary dating: To complement the U-Pb age determinations, a muscovite selvage (sample PAN-XIV-181-1) was dated using the $^{39}Ar/^{40}Ar$ method at the University of Manitoba

599 (Canada) and yielded a good plateau age of 296±2 (1σ) Ma, which is indiscernible within the limits
600 of error (Appendix A7-Table A7) from the preceding $^{39}Ar/^{40}Ar$ age of 296.3±0.6 Ma (1 σ) obtained
601 by Snee et al. (1988) on muscovite selvages. Until now, this age was considered to be the age of the
602 main mineralization (OSS stage of Polya et al., 2000), assuming that this muscovite preceded
603 wolframite deposition. The new results show, however, that the muscovite selvages are at least 2
604 Ma younger.
605
606 **Discussion**
607
608 ***Tourmalinization: one or two fluids?***
609 *Tourmaline as a fluid proxy*
610 According to von Goerne et al. (2001), van Hinsberg (2011), Berryman et al. (2016) and
611 Vereshchagin et al. (2018), the trace element partition coefficients between tourmaline and the
612 medium from which it crystallizes are close to unity. Thus, the relative proportions of the trace
613 elements in tourmaline reflect the relative proportions of trace elements in the fluid from which it
614 crystallized. Fluorine concentration is subject to crystallographic constraints, because of its
615 dependence on the X-charge in the structural formula (Henry and Dutrow, 2011). Within these
616 constraints, the incorporation of F into the tourmaline structure is controlled by external factors, in
617 particular, the F availability, and thus tourmaline may also be considered a F proxy.
618 In the absence of measurable fluid inclusions (FI) in the tourmalinized wall rocks at Panasqueira,
619 information on the nature of the fluids responsible for the tourmalinization can be obtained
620 indirectly, using the tourmaline composition. The major and trace element concentrations differ
621 from Tur1a to Tur1b, pointing to a change in the fluid composition. Consideration of Figure 8-A
622 and 10-A shows a shift from a Co, (Cu), Pb, Sc, Sr, V, Cr, Sn, Nb, Ta package in Tur1a, towards a
623 Li, Fe, Mn, Zn, W rich package in Tur1b. The correlations shown in Figure 13 are clear evidence of
624 a continuous evolution. This evolution could, however, have resulted from either the differentiation
625 of a single fluid or the mixing between two fluid end-members.
626 *Discussion of single fluid models*
627 Single fluid models for the Panasqueira system have been favored by previous workers (Bussink,
628 1984; Lecumberri-Sanchez et al., 2017; Codeço et al., 2017). Codeço et al. (2017) assumed that the
629 Fe# increase was the result of a decrease in the temperature of a single fluid, from ~ 480°-460°C
630 during alteration of the wall rocks to 360°-230°C in the mineralized quartz veins. The former
631 temperature was estimated using the Ti-in-quartz thermometer (Codeço et al., 2017), whereas the
632 latter come from earlier fluid inclusion studies (e.g., Kelly and Rye, 1979). Recent fluid inclusion

633 studies (Dejean, 2017; Cathelineau et al., 2017; 2018; Carocci, 2019) have concluded, however, that
634 the temperature of the main quartz-wolframite deposition stage was 450°±50°C. Therefore, a strong
635 temperature decrease cannot be the explanation for the change in Fe#.
636 Lecumberri-Sanchez et al. (2017) related the wolframite deposition to wall rock alteration. They
637 concluded that the muscovitized parts, which commonly (but not systematically) fringe the
638 mineralized quartz veins were coeval with the more distal tourmalinized zone, and that wolframite
639 deposited due to the interaction of a Fe-poor, but W-bearing fluid, with the schists as a result of the
640 release of Fe from the latter during muscovitization. This model is unsupported because: (1)
641 muscovitization at the vein borders post-dated tourmalinization (see above), (2) the muscovitized
642 fringes formed synchronously with the muscovite selvages of the mineralized quartz veins, and (3)
643 the geochronological data reported in this study show that muscovite formed later than the wall-
644 rock tourmalinization.
645 A fractional crystallization model could explain the Fe# increase from Tur1a to Tur1b but would
646 require that the system was closed, which is inconsistent with the crack-seal textures of the Qcs
647 veinlets associated with fluid influx into the wall rocks. It is difficult to reconcile this model with
648 the differential behavior of the trace elements between Tur1a and Tur1b, some having been
649 enriched, and others impoverished, something which cannot be explained by the effect of
650 differences between partition coefficients. This model also explains the significant overlap of the
651 trace element compositions of Tur1a and Tur1b (Fig. 13).
652 A final single fluid model that could be considered is one in which the system evolved
653 continuously from wall rock-controlled (Tur0) to fluid-controlled (Tur1b stage) conditions during
654 the course of fluid-rock interaction. High water-rock ratios are indicated by the absence of
655 compositional differences in either the Tur1a or Tur1b zones, with respect to the position of
656 tourmaline in the system, irrespective of whether the tourmaline is in Qcs veinlets or part of the
657 tourmalinized wall rock, proximal or distal to the veinlets. Furthermore, the widespread evidence of
658 corrosion of the Tur0 cores points to sudden changes in the ambient fluid composition, which is
659 difficult to reconcile with the single fluid model. During such fluid-rock interaction, the Tur0
660 composition would reflect the host-rock composition prior to the alteration, masking the
661 characteristics of the incoming fluid. Petrographic observations indicate that tourmaline grew at the
662 expense of earlier ferro-magnesian minerals (biotite, cordierite). Thus, the Fe# in the Tur0 cores
663 would be expected to reflect the Fe# of the Beira schist, which is not the case (Fig. 8A). In addition,
664 the lack of F in Tur0 is in strong contrast with the high F content of the Beira schists (570 ppm in
665 average: Oosterom et al., 1984). Also, despite the high Ti content (0.6 to 1.0 wt% TiO_2) of the Beira
666 schists (Bussink, 1984), the tourmaline is Ti-poor, which may, however, be due, at least in part, to

667 competition with the coeval rutile. The Tur1a and Tur1b trace element package is, in order of
668 decreasing abundance (Figure 10-A): Ti-Zn-Mn-(V, Cr)-(Sr,Li)-Sn-(Sc,Ni)-Be-Pb-W-(Cu,Co)-Y-
669 Nb-Ta. A compilation of local data (Figure 10-B) reveals that in the Beira schists, these elements
670 are in a significantly distinct order of decreasing abundance: Ti-Mn-(Zn,V,Li)-(Cr,Sr)-Ni-Cu-
671 (Co,Y,Sc)-Nb-Pb-(W,Sn)-Be-Ta. Therefore, concentrations in Tur0 and Tur1a are not strictly
672 mimetic of the Beira schist composition.
673 In conclusion, no single fluid evolution model is able to fully explain all the data, and a two-fluid
674 model must be seriously considered.
675 *A two-fluid mixing model*
676 We propose a fluid-mixing model involving two end-members, the first of which (F1) was
677 associated with the formation of Tur0, and the second (F2) of which mixed with F1 to form Tur1a
678 and then Tur1b. The F1 fluid end-member composition, like Tur1a, was enriched in Co, (Cu), Pb,
679 Sc, Sr, V, Cr, Sn, Nb, Ta, depleted in F and more magnesian than F2. The F2 fluid end-member
680 composition, like Tur1b, was enriched in Li, Mn, Zn, Fe and F (Fig. 7-D). As tungsten
681 concentration does not correlate with that of Nb, Ta and Sn (Fig. 12 and 13), we propose that it was
682 enriched in the F2 fluid, despite the fact that Tur1b is generally depleted in W relative to Tur1a
683 (Fig. 10-A) and attribute this apparent contradiction to competition for tungsten between Tur1b and
684 the coeval W-rich rutile. This proposal is supported by the abundance of W-bearing nano-inclusions
685 in Tur1b (as inferred from tungsten anomalies in the LA-ICP-MS record, see above) and the
686 occurrence of the coeval W-rich rutile.
687 The fluid-mixing model explains the inter-element correlations and anti-correlations displayed in
688 Figure 13. The corrosion exhibited by the Tur0 core may mark the arrival of F2 into the system and
689 the onset of the mixing process. The evidence for a continuous process and the conflicting evidence
690 of a sharp transition between Tur1a and Tur1b, could indicate a sudden increase in the F2 to F1
691 fluid ratio. This increase could have been related to an interruption in deposition due to a temporary
692 closure of the vein system. Local corrosion, or overprinting (Fig. 9), of Tur1a by Tur1b is a further
693 evidence for this explanation. The small scale oscillations of Fe# during crystal growth, as well as
694 the recurrence of low Fe# at the end of the Tur1b growth, could reflect also temporary variations in
695 the F2 to F1 fluid ratio, explaining the overlap between Tur1a and Tur1b trace element
696 compositions in Figure 13.
697
698 ***The fluid source***
699 *Magmatic or metamorphic source: boron and REE constraints*

Boron: the boron in tungsten deposits is usually considered to be of magmatic origin (e.g., London, 2011), and this interpretation has been adopted for Panasqueira in the recent works of Lecumberri-Sanchez et al. (2017), Codeço et al. (2018) and Launay et al. (2018). According to these studies, fluids released from the Panasqueira granite, and in particular, from the greisenized cupola, provided the boron required for tourmalinization. Codeço et al. (2017) reported that the $\delta^{11}B$ values of the Panasqueira tourmaline are between -4‰ and -13‰ (with 90% of the data between -7‰ and -11‰) and display a Gaussian distribution. These values are consistent with either a magmatic or a metasedimentary source for the boron.

Tourmaline replaced the contact metamorphic aureole minerals related to the emplacement of the main Panasqueira granite, and is therefore later than this magmatic stage. Consequently, tourmalinization is unlikely have been caused by magmatic fluids issued from this large body by itself. In fact, the cupola, as well as the sheet-like body of rare metal granite (RMG) type, at the top of the main granite body (De Amorin, 2017), may have been emplaced later, and, consequently may have been a source of boron, and the fluid to transport it. A mass balance calculation (details presented in Appendix A8) shows that the cupola could not by itself have supplied the quantity of boron needed for wall rock tourmalinization, at the deposit scale. By the same calculation, the subjacent sheet-like RMG body could, however, have supplied a significant part of this boron, although certainly not all that was required. The calculations were done under the assumption of a tourmaline-saturated melt. Yet, tourmaline is typically absent from the cupola or the subjacent RMG, and observation of the cupola/schist contact did not reveal evidence for tourmalinization of the wall rock. The calculated B deliveries are therefore greatly overestimated. Another problem is the volume of fluid that was needed for tourmalinization. The Panasqueira RMG sheet-like body could only have supplied an order of magnitude less than the required volume of fluids (Appendix A8). Another source of boron (and fluids) is clearly required.

Concentrations of boron are around 0.5 to 1%, at tourmaline saturation in aqueous fluids buffered in respect to aluminium silicate at temperatures between 500 and 600°C, according to experimental data (Weisbrod et al., 1986; London, 2011). Consequently, metamorphic fluids may have the capacity to extract and transport boron. The Beira schists contain on average ~ 100 ppm B (Oosterom et al., 1984). Mass balance calculations (Appendix A8) show that the 410 to 810 kt of boron required to account for the observed tourmaline, and the 2.2 to 4.3 km3 of fluid, necessary to dissolve, transport and deposit this amount of boron, may be produced by the devolatilization of no more than 20 km^3 to 40 km^3 of Beira schists.

Rare earth elements: the REE profiles of Tur1 are very similar to those of the Beira schists (Fig. 11), suggesting that the fluids responsible for tourmalinization were of metamorphic origin or

734 equilibrated with metasedimentary rocks at high temperature. Similar REE profiles are observed in
735 tourmaline from deposits for which a metamorphic origin of the fluid is accepted, as for example
736 the orogenic gold deposit of Sarekoubu (Xu et al., 2008) (Fig. 9). In contrast, magmatic-
737 hydrothermal fluids, as well as fluids that equilibrated with granite at a high subsolidus temperature,
738 display a pronounced negative europium anomaly (e.g., Banks et al., 1994; Poitrasson et al., 1995),
739 which is absent from the REE patterns of Panasqueira tourmaline (Fig. 11). A significant magmatic
740 contribution to the tourmalinizing fluids is therefore unlikely.
741
742 *Distinguishing F1-F2 fluids: trace elements constraints*
743 The characteristic Ti, V, Cr, Sr, Sn, Sc, Pb, Ni, Be, Co, Cu, Y, Nb, Ta trace element package
744 deduced for the F1 end-member in a preceding section is consistent with F1 having been
745 equilibrated with a metasedimentary sequence like the Beira Schists. Indeed, it is known that
746 metamorphic fluid compositions reflect those of the related metamorphic rocks (e.g., Tang and Liu,
747 2002).
748 The F2 composition characterized by the Fe, F, Mn, Li, Zn, W package could suggest
749 equilibrium with a granitic magma. Magmatic fluids issued from RMG melts (e.g., Harlaux et al.,
750 2017) rich in F, Li, Fe and Mn, however, are richer in Sn than W, contain similar W and Nb-Ta
751 contents, and are depleted in Zn. These significant differences with the F2 package consequently do
752 not support a magmatic origin for the F2 fluid.
753 This apparent paradox may be resolved in the context of the processes occurring in the CIZ
754 middle crust at the end of the Carboniferous. Dehydration-melting in migmatite domains involving
755 biotite breakdown and the formation of granitic melts (Pereira Gomez et al., 2000) likely took place
756 at the end of the Carboniferous, as in equivalent domains of the Variscan belt at this time (e.g.,
757 Guttierez-Alonso et al., 2011; Barbey et al., 2015). It is known that biotite from the high-grade
758 (unmelted) Beira schists contains significant proportions of F, Li, as well as Fe, Mn, Zn and W
759 (Acosta-Vigil et al., 2011). Biotite breakdown is therefore a potential source for Li, F, Fe, Mn, Zn,
760 and rare metals. The dehydration-melting anatectic domains are also potential sources of large fluid
761 volumes (larger than those released by most granite plutons), produced only through the biotite
762 incongruent melting. During crystallization of the haplogranitic leucosome melt, the unmixed
763 migmatitic fluid would therefore bear the biotite signature in trace elements. This signature, which
764 differs from that of metamorphic fluids issued from unmelted areas, is consistent with the F2 trace
765 element package. Final melting of tourmaline in the anatectic domains delivered boron (Acosta-
766 Vigil et al., 2011), and thus F2 may have contained the boron required for the Tur1b crystallization.
767

768 ***Proposed conceptual model***

769 In order to integrate the preceding results into a workable model for the tourmalinization at
770 Panasqueira, a starting point is to consider the upward transfer of the boron-rich F2 fluid from the
771 inferred source at depth to the deposit level. Here, the concept of a mid-crustal channelized fluid
772 flow (Connolly, 1989) may be called for. According to the modelling by Connolly (1989), deep
773 fluids issued from biotite dehydration gather into a collection zone, and are then focused and
774 channelled into a mid-crustal fault zone, ascending at high rates up to a dispersion region in cooler
775 rocks. The half-width of the collection and dispersion zones is typically in the 3-5 km range, and the
776 height of the system is on the order of 10 to 15 km. The flow results in upward heat advection on a
777 ~ 10^4 yr time-scale, inducing a temperature increase of several 10s °C at the 100 kyr time-scale in
778 the dispersion region (Connolly, 1989).

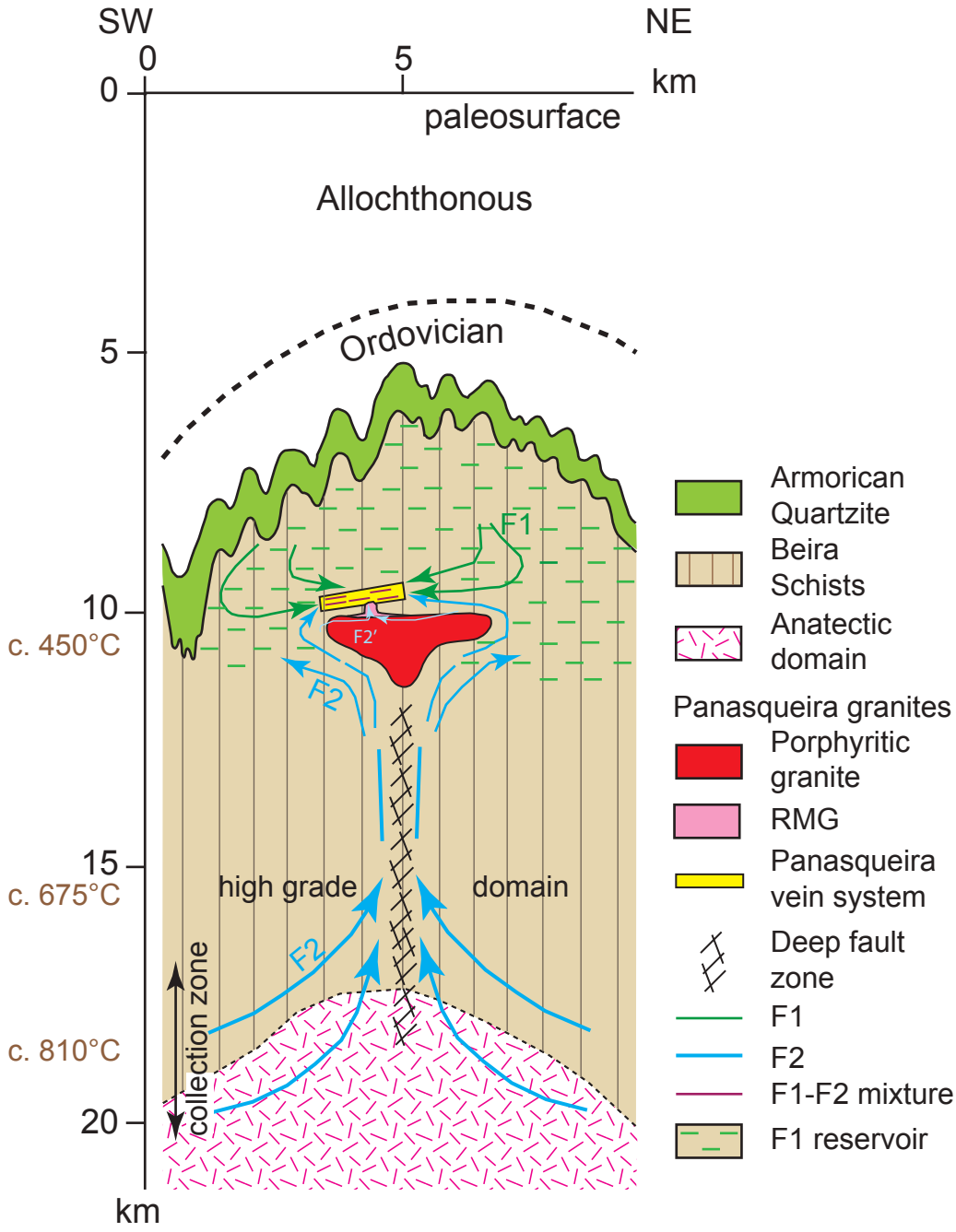

Figure 16. Conceptual model of the crustal scale hydrothermal system at the onset of the main wolframite stage at Panasqueira. A geothermal gradient of ~ 40°C.km^{-1} is assumed (Cathelineau et al., 2018). The model involves two sources of metamorphic fluids at different structural levels (F1 and F2), and their mixing in the Panasqueira vein system. Explanations in the text.

Applied to the Panasqueira system, the collection domain of this model could have been located at depths of 15-20 km, where F2 fluids could have been generated by incongruent melting of biotite. With a total width of 10 km, such a collection domain would have been large enough to provide both the required mass of boron and the fluid volume for tourmalinization. The fault zone necessary for the channelling is thought to have been related to the emplacement of the main

790 Panasqueira granite. Owing to the NNW-SSE elongation of the body (Ribeiro, 2017), this
791 postulated fault should have a similar direction. In addition, fluid ascent was facilitated by the
792 vertical permeability (S_0 and schistosity) in the core of the Panasqueira anticline.
793 At a level corresponding roughly to the bottom of the dispersion level of Connolly (1989), the
794 ascending F2 fluid encountered the Panasqueira granite body and was forced around it, as a
795 consequence of the thermal boundary layer hindering penetration of the flowing fluids into the
796 granite body (this implies that the initiation of the hydrothermal system immediately succeeded
797 granite emplacement). Thereafter, it was driven towards the main permeability channel (the system
798 of joints that guided the future vein system), where it met the resident fluid. As seen in Figure 16, at
799 c. 305 Ma, a continuous cap of thick impermeable Ordovician quartzite (Armorican Quartzite)
800 covered the Beira schists, defining a reservoir for the metamorphic fluids released by either the first
801 LP-HT event in the CIZ at c. 320-317 Ma or by the contact metamorphism of the main Panasqueira
802 granite or both. These fluids are interpreted to represent the F1 end-member. The continuous
803 transfer of heat by the F2 fluid and the resulting heating of the dispersion zone (Connolly, 1989), is
804 thought to have driven convective flow of F1 in the Panasqueira reservoir, promoting the mixing of
805 F1 with F2 fluids in the high permeability domain, which resulted in tourmaline deposition (Fig.
806 16). Cooling of the Panasqueira granite pluton, could have contributed to the thermal anomaly.
807 Launay et al. (2018) described an outwardly flow pattern in the close vicinity of the "greisen
808 cupola", which they interpreted as the radial flow of magmatic fluids out from the cupola. As
809 suggested in Figure 16, this remarkable pattern could as well have resulted from the limited
810 penetration of the F2 fluid in the uppermost granite layers (F2' pattern in Figure 16). Because the
811 F2 input may have varied with time, the model in Figure 16 is consistent with the short-term
812 variations in the F1 to F2 ratios that are inferred from the rutile zoning and tourmaline profiling.
813
814 **Conclusions**
815
816 **1**. The earliest hydrothermal event in the Panasqueira system was wall rock tourmalinization.
817 Zoned tourmaline replaced ferro-magnesian minerals in the protolith in a Tur0-Tur1a,b sequence.
818 This event coincided with the first fluid-overpressure-induced opening of crack-seal fractures (Qcs
819 veinlets).
820 **2**. The early Tur1 tourmaline, and in particular, the development of Tur1b rims, was coeval with
821 the formation of W-bearing rutile (which is among the richest in W anywhere) and the first
822 appearance of wolframite.

823 **3**. On the basis of a limited number of observations, it seems that there is a correlation between
824 the presence/abundance of wolframite in quartz veins and the relative importance in the adjacent
825 altered wall rock of Tur1b rims, and a high content of tungsten in rutile. The poor development of
826 the Tur1b rim, and limited W enrichment in the rutile, together with the presence of ilmenite
827 lamellae, are indicators of barren veins. This is of potential interest for evaluating exploration drill
828 holes from a resource and mine development perspective.
829 **4**. The early rutile crystallized at 305.2 ± 5.7 Ma and coincided with early tourmalinization and
830 the first appearance of wolframite. This new age is greater than the currently accepted age of c. 296
831 Ma, which was obtained on muscovite selvages that post-dated wolframite deposition.
832 **5**. The Panasqueira hydrothermal system was active for more than 6-8 Ma and was the product
833 of a much deeper crustal system than proposed in previous studies, in which the W mineralizing
834 fluids were released by a single granite intrusion.
835 **6**. Two fluids, both of metamorphic origin, were involved in tourmaline growth. The first, rich in
836 Ti, V, Cr, Sr, Sn, Sc, Pb, Ni, Co, Cu, Y, Nb, Ta, and of "local" derivation, was replaced
837 progressively by a second fluid, rich in Li, F, Fe, Mn, W, of deeper origin (biotite dehydration).
838 This second fluid carried the metals necessary for wolframite deposition and in particular Fe and
839 Mn, which were not inherited from the host rocks.
840
841 **Acknowledgements**
842 EG Berryman and in particular AE William-Jones are thanked for constructive criticism and
843 detailed suggestions that helped to improve the first drafts of the manuscript. Additional corrections
844 from F. B. Wadsworth (Durham University) and A. Samper (OTELO, Lorraine University) were
845 greatly appreciated.
846 This work benefited from the analytical capabilities of the GeoRessources Laboratory
847 (Université de Lorraine, CNRS, CREGU), and the authors gratefully acknowledge Olivier Rouer,
848 Andrei Lecomte, Lise Salsi and Chantal Peiffert for their technical help. LA-ICP-MS equipment
849 was financed by CPER program (National Funds – Lorraine region – FEDER).
850 This work was financed by the ERAMIN project NewOres financed by ANR (ANR-14-EMIN-
851 0001), and Labex Ressources 21 (supported by the French National Research Agency through the
852 national program "Investissements d'avenir") with reference ANR – 10 – LABX 21 —LABEX
853 RESSOURCES 21.
854 We are most grateful to Beralt Tin and Wolfram S.A. for permitting access to the Panasqueira
855 underground mine, and technical help during field work.
856

857 **References**

858

859 Acosta-Vigil, A., Pereira, M.D., Shaw, D.M., and London, D., 2011, Contrasting behaviour of
860 boron during crustal anatexis: Lithos, v. 56, p. 15-31.

861 Alcock, J.E., Martínez Catalán, J.R., Rubio Pascual F.-J., Díez Montes, A., Díez Fernández, R.,
862 Gómez Barreiro, J., Arenas, R., Dias da Silva, I., and Clavijo, E.G., 2015, 2-D thermal
863 modeling of HT–LP metamorphism in NW and Central Iberia: Implications for Variscan
864 magmatism, rheology of the lithosphere and orogenic evolution: Tectonophysics, v. 657, p.
865 21-37.

866 Almonty Industries, 2016, Report NI 43-101. Technical report on the mineral resources and
867 reserves of the Panasqueira mine, Portugal: http://www.almonty.com
868 /_resources/Panasqueira_43-101_Tech_Rep_Dec16_SEDAR.PDF.

869 Banks, D.A., Yardley, B.W.D., Campbell, A.R., and Jarvis, K.E., 1994, REE composition of an
870 aqueous magmatic fluid: A fluid inclusion study from the Capitan Pluton, New Mexico,
871 U.S.A: Chemical Geology, v. 113, p. 259-272.

872 Barbey, P., Villaros, A., Marignac, C., and Montel, J.M., 2015, Multiphase melting, magma
873 emplacement and P-T-time path in late-collisional context: the Velay example (Massif
874 Central, France): Bulletin de la Société Géologique de France, v. 186, p. 93–116.

875 Berryman, E.J., Kutzschbach, M., Trumbull, R.B., Meixner, A., van Hinsberg, V., Kasemann, S.A.,
876 and Frantz, G., 2017, Tourmaline as a petrogenetic indicator in the Pfitsch Formation,
877 Western Tauern Window, Eastern Alps: Lithos, v. 284-285, p. 138-155.

878 Bloot, C., and De Wolf, L.C.M., 1953, Geological features of the Panasqueira tin-tungsten ore-
879 occurrence (Portugal): Boletim da Sociedade Geologica de Portugal, v. XI, p. 1-57.

880 Bosi, F., 2011, Stereochemical constraints in tourmaline: from a short-range to a long-range
881 structure: The Canadian Mineralogist, v. 49, p. 17-27.

882 Bosi, F., 2018, Tourmaline crystal chemistry: American Mineralogist, v.103, p. 298-306.

883 Burnard, P.G., and Polya, D.A., 2004, Importance of mantle derived fluids during granite associated
884 hydrothermal circulation: He and Ar isotopes of ore minerals from Panasqueira: Geochimica
885 et Cosmochimica Acta, v. 68, p. 1607–1615. doi:10.1016/j.gca.2003.10.008.

886 Bussink, R.W., 1984, Geochemistry of the Panasqueira tungsten-tin deposit, Portugal: Geologia
887 Ultraiectina, v. 33, p. 1-159.

888 Carocci, E., 2019, Tungsten transport ad deposition in magmatic-hydrothermal environments : the
889 example of Panasqueira (Portugal): PhD Thesis, Univ. de Lorraine, 271 p.

890 Carocci E., Marignac C., Cathelineau M., Truche L., Lecomte A., and Pinto F., 2019, Rutile from
891 Panasqueira (Central Portugal): an excellent pathfinder for wolframite deposition: Minerals,
892 v. 9, 9; https://doi.org/10.3390/min9010009.
893 Castro, A., Corretge, L.G., de la Rosa, J.D., Fernández, C., López, S., García-Moreno, O., and
894 Chacón, H., 2003, The appinite–migmatite complex of Sanabria, NW Iberian Massif, Spain:
895 Journal of Petrology, v. 44, p. 1309–1344.
896 Cathelineau, M., Marignac, C., Rolland, J.-M., Boiron, M.-C., and Dejean, M., 2017, Are we sure to
897 know the fluids responsible for W mineralization at Panasqueira (Portugal): the case for loss
898 of information due to intense quartz recrystallization and FI natural decrepitation: European
899 Current Research on Fluid Inclusions (ECROFI) Biennial Meeting, 24th, Nancy, France,
900 Abstracts, p. 98.
901 Cathelineau, M., Marignac, C., Boiron, M.-C, Carocci, E., Rolland, J.-M., Dejean, M, Dourk, M.,
902 and Pinto, F., 2018, Nouvelle approche du chemin P-T-t des fluides dans le gisement à W-Sn-
903 Cu de Panasqueira (Portugal): persistence d'une anomalie thermique d'origine profonde en
904 cours d'exhumation: Earth Science Meeting (RST), 26th, Lille, France, 2018, Abstracts, p.
905 694.
906 Chew, D.M., Petrus, J.A., and Kamber, B.S., 2014, U-Pb LA-ICPMS dating using accessory
907 mineral standards with variable common Pb: Chemical Geology, v. 363, p. 185-199.
908 Clark, A.H., 1970, Potassium-argon ages and regional relationships of the Panasqueira tin-tungsten
909 mineralization, Portugal: Servicos Geologicos Comunicacoes, v. 54, p. 243-261.
910 Codeço, M.S., Weis, P., Trumbull, R.B., Pinto, F., Lecumberri-Sanchez, P., and Wilke, F.D., 2017,
911 Chemical and boron isotopic composition of hydrothermal tourmaline from the Panasqueira
912 W-Sn-Cu deposit, Portugal: Chemical Geology, v. 468, p. 1-16.
913 Connolly, J.A.D., 1989, Mid-crustal focused fluid movement: thermal consequences and silica
914 transport, in Jamtveit, B., Yardley, B.W.D., eds, Fluid flow and transport in rocks,
915 mechanisms and effects: Chapman & Hall, London, p. 235-250.
916 De Amorin, A., 2017, Pétrographie géochimie des granitoides de la mine de W de Panasqueira
917 (Portugal): Rôle dans la genèse des minéralisations: Unpublished M.Sc. thesis, Université de
918 Lorraine (France), Laboratoire Géoressources, 37 p.
919 Dejean, M., 2017, Fluides minéralisateurs dans le gisement de Panasqueira: Reconstruction P-T-X:
920 Master2 Univ de Lorraine, 31 p.
921 Dias, G., Leterrier, J., Mendes, A., Simões, P.P., and Bertrand J.M., 1998, U-Pb zircon and
922 monazite geochronology of post-collisional Hercynian granitoids from the Central Iberian
923 Zone (Northern Portugal): Lithos, v. 45, p. 349-369.

924 Díez Fernández, R., and Pereira, M.F., 2017, Strike-slip shear zones of the Iberian Massif: Are they
925 coeval?: Lithosphere, v. 9, p. 726-744.
926 Díez Fernández, R., Martínez Catalán, J.R., Barreiro, J.G., and Arenas, R., 2012, Extensional Flow
927 during Gravitational Collapse: A Tool for Setting Plate Convergence (Padrón Migmatitic
928 Dome, Variscan Belt, NW Iberia): The Journal of Geology, v. 120, p. 83-103.
929 Díez Fernández, R., Barreiro, J.G., Martínez Catalán, J.R., and Ayarza, P., 2013, Crustal thickening
930 and attenuation as revealed by regional fold interference patterns: Ciudad Rodrigo basement
931 area (Salamanca, Spain): Journal of Structural Geology, v. 46, p.115-128.
932 Díez Fernández, R., Arenas, R., Pereira, M.F., Sánchez-Martínez, S., Albert, R., Martin Parra, L.M.,
933 Rubio Pascual, F.J., and Matas, J., 2016, Tectonic evolution of Variscan Iberia: Gondwana–
934 Laurussia collision revisited: Earth-Science Reviews, v. 162, p. 269-292.
935 Fernández-Suárez, J., G. Gutiérrez-Alonso, S. T. Johnston, T. E. Jeffries, D. Pastor-Galan, G. A.
936 Jenner, and Murphy, J.B., 2011, Iberian late- Variscan granitoids: Some considerations on
937 crustal sources and the significance of "mantle extraction ages": Lithos, v. 123, p. 121–132,
938 doi:10.1016/ j.lithos.2010.09.010.
939 Foxford, K.A., Nicholson, R., and Polya, D.A., 1991, Textural evolution of W–Cu–Sn bearing
940 hydrothermal quartz veins at Minas da Panasqueira, Portugal: Mineralogical Magazine, v. 55,
941 p. 435–445.
942 Foxford, K.A., Nicholson, R., Polya, D.A., and Hebblethwaite, R.P.B., 2000, Extensional failure
943 and hydraulic valving at Minas da Panasqueira, Portugal: evidence from vein spatial
944 distributions, displacements and geometries: Journal of Structural Geology, v. 22, p. 1065–
945 1086, http://dx.doi.org/10.1016/S0191-8141(00)00029-8.
946 Garcia, D., 2004, Travaux présentés pour l'obtention du diplôme Habilitation à Diriger les
947 Recherches en Sciences de la Terre et de l'Univers, Espace: Génie des procédés, Université
948 Jean Monnet; Ecole Nationale Supérieure des Mines de Saint-Etienne, 87 p.
949 Guttiérrez-Alonso, G., Fernández-Suárez, J., Jeffries, T.E., Johnston, S.T., Pastor-Galán, D.,
950 Murphy, J.B., Franco, P., and Gonzalo, J.C., 2011, Diachronous post-orogenic magmatism
951 within a developing orocline in Iberia, European Variscides: Tectonics, v 30,
952 doi:10.1029/2010TC002845.
953 Harlaux, M, 2016, Les systèmes métallogéniques hydrothermaux à tungstène et métaux rares (Nb,
954 Ta, Sn) dans le contexte orogénique fini-varisque : exemple du Massif Central Français)
955 (Tungsten and rare-metal (Nb, Ta, Sn) hydrothermal metallogenic systems in the late-
956 Variscan orogenic context: example of the French Massif Central): PhD thesis, Université de
957 Lorraine (France), Laboratoire Géoressources, 451 p.

Harlaux, M., Mercadier, J., Bonzi, W.M.-E., Kremer, V., Marignac, C., and Cuney, M., 2017, Geochemical signature of magmatic-hydrothermal fluids exsolved from the Beauvoir rare-metal granite (Massif Centra, France): insights from LA-ICPMS analysis of primary fluid inclusions: Geofluids, v. 2017, Article ID 1925817, 25 p. https ://doi.org/10.1155/2017/1925817.

Hawthorne, F.C., and Dirlam, D.M., 2011, Tourmaline the indicator mineral: From atomic arrangement to Viking navigation: Elements, v. 7, p. 307-312.

Henry, D.J., and Dutrow, B.L., 2011, The incorporation of fluorine in tourmaline: internal crystallographic controls or external environmental influence?: The Canadian Mineralogist, v. 49, p. 41-56.

Henry, D.J., and Guidotti, C.V., 1985, Tourmaline as a petrogenetic indicator mineral: an example from the staurolite-grade metapelites of NW Maine: American Mineralogist, v. 70, p. 1-15.

Henry, D.J., Novák, M., Hawthorne, F.C., Ertl, A., Dutrow, B.L., Uher, P., and Pezzotta, F., 2011, Nomenclature of the tourmaline supergroup minerals: American Mineralogist, v. 96, p. 895–913.

Inverno, C.M.C., Ferraz, P.J.V., and Moreira, E., 2009, Argemela, a high-tonnage Sn-Li deposit in Central Portugal: Geological Society of America Annual Meeting, Portland, 2009, Abstracts 41, p. 680.

Jacques, D., Vieira, R., Muchez, P., and Sintubin, M., 2018, Transpressional folding and associated cross-fold jointing controlling the geometry of post-orogenic vein-type W-Sn mineralization: examples from Minas da Panasqueira, Portugal: Mineralium Deposita, v. 53, p. 171-194.

Jaques, L., and Pascal, C., 2017, Full paleostress tensor reconstruction using quartz veins of Panasqueira Mine, central Portugal; part I: Paleopressure determination: Journal of Structural Geology, v. 102, p. 58-74.

Julivert, M., Fontboté, J.M., Ribeiro, A., and Nabais-Conce, L.E., 1972, Mapa tectónico de la Península Ibérica y Baleares, 1:1.000.000: IGME, Memoria explicativa, p. 113.

Kelly, W.C., and Rye, R.O., 1979, Geologic, fluid inclusion, and stable isotope studies of the tin–tungsten deposits of Panasqueira, Portugal: ECONOMIC GEOLOGY, v. 74, p. 1721–1822.

Kuhn, T., 2018, Al-in-Hornblende barometry of Southern New England intrusions and comparison with metamorphic bathograds: Senior Thesis, Department of Geology and Geophysics, Yale University, 25 p.

Lach P, Mercadier J., Dubessy J., Boiron M.C., Cuney M., 2013, In-situ quantitative measurement of rare earth elements in uranium oxides by Laser Ablation-Inductively Coupled Plasma-Mass Spectrometry. Geostandards and Geoanalytical Research. 37, 277-296

992 Launay, G., Sizaret, S., Guillou-Frottier, L., Gloaguen, E., and Pinto, F., 2018. Deciphering fluid
993 flow at the magmatic-hydrothermal transition: A case study from the world-class Panasqueira
994 W–Sn–(Cu) ore deposit (Portugal): Earth and Planetary Science Letters, v. 499, p. 1-12.
995 Lecumberri-Sanchez, P., Vieira, R., Heinrich, C., Pinto, F., and Walle, M., 2017, Fluid-rock
996 interaction is decisive for the formation of tungsten deposits: Geology, vol. 45, p. 579–582.
997 Leisen M., Dubessy J., Boiron M.C., Lach P., 2012. Improvement of the determination of element
998 concentrations in quartz-hosted fluid inclusions by LA-ICP-MS and Pitzer thermodynamic
999 modeling of ice melting temperature. Geochim. Cosmochim. Acta, 90, 110-125.
1000 Lewis, A.J., Palmer, M.R., Sturchio, N.C., and Kemp, A.J., 1997, The rare earth element
1001 geochemistry of acid-sulphate and acid-sulphate-chloride geothermal systems from
1002 Yellowstone National Park, Wyoming, USA: Geochimica et Cosmochimica Acta, v. 61, p.
1003 695-706.
1004 Linnen, R.L., and Cuney, M., 2005, Granite-related rare-element deposits and experimental
1005 constraints on Ta-Nb- W-Sn-Zr-Hf mineralization, in Linnen, R.L. and Samson, I.M., eds.,
1006 rare-element geochemistry and mineral deposits, Geological Association of Canada, Short
1007 Course Notes, v. 17, p. 45-67.
1008 Llana-Funez, S., and Marcos, A., 2007, Convergence in a thermally softened thick crust: Variscan
1009 intracontinental tectonics in Iberian plate rocks: Terra Nova, v. 19, p. 1-8.
1010 London, D., 2011, Experimental synthesis and stability of tourmaline: a historical overview: The
1011 Canadian Mineralogist, v. 49, p. 117-136.
1012 Lourenço, A., 2002, Paleofluidos e mineralizações associadas às fases tardias da Orogenia
1013 Hercínica: Unpublished PhD, Universidade do Porto, 326 p.
1014 Lüders, V., 1996, Contribution of infrared microscopy to fluid inclusion studies in some opaque
1015 minerals (wolframite, stibnite, bournonite): Metallogenic implications: ECONOMIC
1016 GEOLOGY, v. 91, p. 1462–1468.
1017 Ludwig, K.R., 2012, User's Manual for Isoplot 3.75, A Geochronological Toolkit for Microsoft
1018 Excel: Berkeley Geochronology Center, Special Publication No. 5.
1019 Luvizotto, G.L, Zack, T., Meyer, H.P., Ludwig, T., Triebold, S., Kronz, A., Münker, C., Stockli,
1020 D.F., Prowatke, S., Klemme, S., Jacob, D.E., and von Eynatten, H., 2009, Rutile crystals as
1021 potential trace element and isotope mineral standards for microanalysis: Chemical Geology,
1022 v., 261, p. 346-369.
1023 Marignac, C., Cuney, M. (2013) Past and present rare metal potential of Western Europe: In: PDAC
1024 2013 (Toronto) Short Course "New Mines in the Old World: the untapped potential of
1025 Europe".

1026 Marschall, H.R., and Jiang, S-Y., 2011, Tourmaline isotopes: No element left behind: Elements, v.
1027 7, p. 313-319.
1028 Mateus, A., and Noronha, F., 2010, Sistemas mineralizantes epigenéticos na Zona Centro-Ibérica;
1029 expressão da estruturação orogénica meso- a tardi-varisca (Epigenetic ore-forming systems in
1030 Central-Iberian Zone; products of an evolving orogenic framework in meso- to late-Variscan
1031 times): Ciências Geológicas, Ensino, Investigação e sua História (Geologia Aplicada), v. 2, p.
1032 47-61.
1033 Michaud J.A.-S., Gumiaux C, Pichavant, M., Gloaguen, E., Marcoux, E., 2020, From magmatic to
1034 hydrothermal Sn-Li-(Nb-Ta-W) mineralization: The Argemela area (central Portugal): Ore
1035 Geology Reviews, v. 116, https: // doi.org/ 10.1016/ j.oregeorev.2019.103215
1036 Nägler, T.F., Schäfer, H-J., and Gebauer, D., 1993, A new approach for the determination of the age
1037 of partial or complete homogenization of Pb isotopes Example: anchimetamorphic, detrital
1038 sediments of the Central Iberian Zone, Spain: Chemical Geology, v. 107, p. 191-199.
1039 Nägler, T.F., Schäfer, H-J., and Gebauer, D., 1995, Evolution of the Western European continental
1040 crust: implications from Nd and Pb isotopes in Iberian sediments: Chemical Geology, v. 121,
1041 p. 345-357.
1042 Neiva, A.M.R., 2002, Portuguese granites associated with Sn-W and Au mineralizations: Bulletin
1043 of the Geological Society of Finland, v. 74, p. 79-101.
1044 Neiva, A.M.R., Silva, M.M.V.G., and Gomes, M.E.P., 2007, Crystal chemistry of tourmaline from
1045 Variscan granites, associated tin-tungsten- and gold deposits, and associated metamorphic and
1046 metasomatic rocks from northern Portugal: Neues Jahrbuch für Mineralogie Abhandlungen, v.
1047 184, p. 45-76.
1048 Noronha, F., 2017, Fluids and Variscan metallogenesis in granite related systems in Portugal:
1049 Water-Rock Interaction International Symposium, 15th: Procedia Earth and Planetary Science,
1050 v. 1, p. 1-4.
1051 Noronha, F., Dória, F., Dubessy, J., and Charoy, B., 1992, Characterization and timing of the
1052 different types of fluids present in the barren and ore veins of the W–Sn deposit of
1053 Panasqueira, central Portugal: Mineralium Deposita, v. 27, p. 72–79.
1054 Oosterom, M.G., Bussink, R.W., and Vriend, S.P., 1984, Lithogeochemical studies of aureoles
1055 around the Panasqueira tin-tungsten deposit, Portugal: Mineralium Deposita, v. 19, p. 283-
1056 288.
1057 Orejana, D., Villaseca, C., Pérez-Soba, C., López-García, J.A., and Billström, K., 2009, The
1058 Variscan gabbros from the Spanish Central System: A case for crustal recycling in the sub-
1059 continental lithospheric mantle?: Lithos, v. 110, p. 262-276.

1060 Paquette, J.L., Piro, J.-L., Devidal, J-L., Bosse, V., Didier, A., Sannac, S., and Abdelhour, Y., 2014,
1061 Sensivity enhancement in LA-ICP-MS by N_2 addition to carrier gas: application to
1062 radiometric dating of U-Th -bearing minerals: Agilent ICP-MS Journal, v. 58, p; 4-5.
1063 Paton, C., Hellstrom, J., Bence, P., Woodhead, J., and Herg, J., 2011, Iolite: Freeware for the
1064 visualisation and processing of mass spectrometric data: Journal of Analytical Atomic
1065 Spectrometry, v. 26, p. 2508-2518.
1066 Pattison, D.R.M., 2001, Instability of Al2O5 'triple point' assemblages in muscovite+biotite+quartz
1067 bearing metapelites, with implications: American Mineralogist, v. 86, p. 1414-1422.
1068 Pereira, M.F., Díez Fernández, R., Gama, C., Hofmann, M., Gärtner, A., and Linnemann, U., 2017,
1069 S-type granite generation and emplacement during a regional switch from extensional to
1070 contractional deformation (Central Iberian Zone, Iberian autochthonous domain, Variscan
1071 Orogeny): International Journal of Earth Sciences (Geologische Rundschau), DOI
1072 10.1007/s00531-017-1488-3.
1073 Pereira Gómez, M.D., and Rodriguez Alonso, M.D., 2000, Duality of cordierite granites related to
1074 melt-restite segregation in the Peña Negra anatectic complex, central Spain: Canadian
1075 Mineralogy, v. 38, p. 1329-1346.
1076 Pérez-Cáceres, I., Martínez Poyatos, D., Fernando Simancas, J., and Azor, A., 2017, Testing the
1077 Avalonian affinity of the South Portuguese Zone and the Neoproterozoic evolution of SW
1078 Iberia through detrital zircon populations: Gondwana Research, v. 42, p. 177-192.
1079 Pinto, F., 2014, Estudo da distribuição do Estanho na Mina da Panasqueira: Mestrado em Geologia,
1080 FCUP, Departamento de Geociências, Ambiente e Ordenamento do Território, 236 p.
1081 Poitrasson, F., Pin, C., and Duthou, J-L., 1995, Hydrothermal remobilization of rare earth elements
1082 and its effect on Nd isotopes in rhyolite and granite: Earth and Planetary Science Letters, v.
1083 130, p. 1-11.
1084 Polya, D.A., 1989, Chemistry of the main-stage ore-forming fluids of the Panasqueira W–Cu(Ag)–
1085 Sn deposit, Portugal: implications for models of ore genesis: ECONOMIC GEOLOGY, v. 84,
1086 p. 1134–1152.
1087 Polya, D.A., Foxford, K.A., Stuart, F., Boyce, A., and Fallick, A.E., 2000, Evolution and
1088 paragenetic context of low δD hydrothermal fluids from the Panasqueira W-Sn de- posit,
1089 Portugal: new evidence from microthermometric, stable isotope, noble gas and halogen
1090 analyses of primary fluid inclusions: Geochimica et Cosmochimica Acta, v. 64, p. 3357–
1091 3371.

1092 Priem, H.N.A., and Den Tex, E., 1984, Tracing crustal evolution in the NW Iberian Peninsula
1093 through the Rb-Sr and U-Pb systematics of Paleozoic granitoids: a review: Physics of the
1094 Earth and Planetary Interiors, v. 35, p. 121-130.
1095 Renne, P.R., and Norman, E.B., 2001, Determination of the half-life of Ar-37 by mass
1096 spectrometry: Physical Review, v. C, p. 6304-7302.
1097 Renne, P.R., Swisher, C.C., Deino, A.L., Karner, D.B., Owens, T.L., and DePaolo, D.J., 1998,
1098 Inter-calibration of standards, absolute ages and uncertainties in 40Ar/39Ar dating: Chemical
1099 Geology, v. 145, p. 117-152.
1100 Renne, P.R., Cassata, W.S., and Morgan, L.E., 2009. The isotopic composition of atmospheric
1101 argon and 40Ar/39Ar geochronology: Time for a change?: Quaternary Geochronology, v. 4,
1102 p. 288–298.
1103 Ribeiro, R.F., 2017, Gravimetric Modelling and Geological Interpretation of Argemela-Panasqueira
1104 Area: PhD Thesis, Porto Universidad, 61 p.
1105 Roddick, J.C., 1983, High precision intercalibration of $^{40}Ar/^{39}Ar$ standards: Geochimica et
1106 Cosmochimica Acta, v. 47, p. 887-898.
1107 Rubio Pascual, F.J., Arenas, R., Martínez Catalán, J.R., Rodríguez Fernández, L.R., and Wijbrans,
1108 J.R., 2013, Thickening and exhumation of the Variscan roots in the Iberian Central System:
1109 Tectonothermal processes and $^{40}Ar/^{39}Ar$ ages: Tectonophysics, v. 587, p. 207-221.
1110 Rubio Pascual, F.J., López-Carmona, A., and Arenas, R., 2016, Thickening vs. extension in the
1111 Variscan belt: P–T modelling in the Central Iberian autochthon: Tectonophysics, v. 681, p.
1112 144-158.
1113 Sant'Ovaia, H., Olivier, P., Ferreira, N., Noronha, F., and Leblanc, D., 2010, Magmatic structures
1114 and kinematics emplacement of the Variscan granites from Central Portugal (Serra da Estrela
1115 and Castro Daire areas): Journal of Structural Geology, v. 32, p. 1450-1465.
1116 Scarrow, J.H., Molina, J.F., Bea, F., Montero, P., and Vaughan, A.P.M., 2011, Lamprophyre dikes
1117 as tectonic markers of late orogenic transtension timing and kinematics: A case study from the
1118 Central Iberian Zone: Tectonics, v, 30(4): TC4007.
1119 Sluck, J.F., and Trumbull, R.B., 2011, Tourmaline as a recorder of ore-forming processes:
1120 Elements, v. 7, p. 321-366.
1121 Snee, L.W., Sutter, J.F., and Kelly, W.C., 1988, Thermochronology of economic mineral deposits:
1122 dating the stages of mineralisation at Panasqueira, Portugal, by high-precision ^{40}Ar-^{39}Ar age
1123 spectrum techniques on muscovite: ECONOMIC GEOLOGY, v. 83, p. 335-354.
1124 Stacey, J.S., and Kramers, J.D., 1975, Approximation of terrestrial lead isotope evolution by a two-
1125 stage model: Earth and Planetary Science Letters, v. 26, p. 207–221.

1126 Steiger, R.H., and Jäger, E., 1977, Subcommission on geochronology: Convention on the use of
1127 decay constants in geo- and cosmochronology: Earth and Planetary Science Letters, v. 36, p.
1128 359–362, doi: 10.1016/0012-821X(77)90060-7.
1129 Tang, H.-F., and Liu, C.-Q., 2002, Trace element geochemistry during metamorphic dehydration: A
1130 case study from the Xingzi Group of Lushan, southeast China: Geochemical Journal, v.36, p.
1131 545-561.
1132 Tornos, F., Delgado, A., Casquet, C., and Galindo, C., 2000, 300 Million years of episodic
1133 hydrothermal activity: stable isotope evidence from hydrothermal rocks of the eastern Iberian
1134 Central System: Mineralium Deposita, v. 35, p. 551–569.
1135 Valladares, M.I., Ugidos, J.M., Barba, P., and Colmenero, J.R., 2002,Contrasting geochemical
1136 features of the Central Iberian Zone shales (Iberian Massif, Spain): implications for the
1137 evolution of Neoproterozoic–Lower Cambrian sediments and their sources in other peri-
1138 Gondwanan areas: Tectonophysics, v. 352, p. 121-132.
1139 van Hinsberg, V.J., 2011, Preliminary experimental data on trace-element partitioning between
1140 tourmaline and silicate melt: The Canadian Mineralogist, v. 49, p. 153-163
1141 van Hinsberg, V.J., Henry, D.J., and Marschall, H.R., 2011, Tourmaline: an ideal indicator of its
1142 host environment: The Canadian Mineralogist, v. 49, p.1-16.
1143 Vereshchagin, O.S., Frank-Kamenetskaya, O.V., Rozhdestvenskaya, I.V., and Zolotariev, A.A.,
1144 2018, Incorporation of 3*d* elements in tourmalines: structural adjustments and stability:
1145 European Journal of Mineralogy, v. 30, p. 917-928.
1146 Vermeesch, P., 2012, On the visualisation of detrital age distributions: Chemical Geology, v. 312-
1147 313, p. 190-194, doi: 10.1016/j.chemgeo.2012.04.021.
1148 Vigne, J-L., André, G., and Kapal, F., 2018, Données industrielles, économiques, géographiques sur
1149 les principaux produits chimiques, métaux, matériaux (11ème edition).
1150 http://www.societechimiquedefrance.fr/extras/Donnees/acc.htm
1151 von Goerne, G., Franz, G., and Heinrich, W., 2001, Synthesis of tourmaline solid solutions in the
1152 system Na_2O ±MgO ±Al_2O_3 ±SiO_2 ±B_2O_3 ±H_2O ±HCl and the distribution of Na between
1153 tourmaline and fluid at 300 to 700 °C and 200 MPa: Contributions to Mineralogy and
1154 Petrology, v. 141, p. 160-173.
1155 Weil, A.B., Gutiérrez-Alonso, G., Johnston, S.T., Pastor-Galán, D., 2013, Kinematic constraints on
1156 buckling a lithospheric-scale orocline along the northern margin of Gondwana: A geologic
1157 synthesis: Tectonophysics, v. 582, p. 25-49.
1158 Weisbrod, A., Polak, C., and Roy, D., 1986, Experimental study of tourmaline solubility in the
1159 system Na–Mg–Al–Si–B–O–H. Applications to the boron content of natural hydrothermal

fluids and tourmalinization processes: International Symposium on Experimental Mineralogy and Geochemistry, Nancy, 1986, Abstracts, v. 140-141.

Xu, J., Ding, R., Xie, Y., Zhong C., and Shan L., 2008, The source of hydrothermal fluids for the Sarekoubu gold deposit in the southern Altai, Xinjiang, China: Evidence from fluid inclusions and geochemistry: Journal of Asian Earth Sciences, v. 32, p. 247-258.

Zack, T., Stockli, D.F., Luvizotto, G.L., Barth, M.G., Belousova, E., Wolfe, M.R., and Hinton, R.W., 2011, In situ U-Pb rutile dating by LA-ICP-MS: ^{208}Pb correction and prospects for geological applications: Contributions to Mineralogy and Petrology, DOI 10.1007/s00410-011-0609-4

Appendix A0. Comparaison of SEM-EDS and EPMA analyses of Panasqueira tourmaline

1. Problems in measuring Tur compositions by EPMA

The Pnq tourmaline crystals from the tourmalinized wall rocks are very small and therefore so are the different zones in the crystals. Owing to the rather low contrasting capacity of back scatter imaging by EPMA in our laboratory, it is usually challenging to assure that a given spot is really located in the desired zone: this is particularly true for the Tur 0 residual cores, that are usually not seen with EPMA. What is more, it is not so easy to retrieve under EPMA the crystals imaged by SEM - given that we ordinary explore the sections at random to find the best crystals.

For all these reasons, it was desirable to make measurements while identifying the zoning features, i.e., to mainly use SEM-EDS. To ensure compatibility of the two approaches, EPMA and SEM measurement were both performed on chosen crystals. Comparison between the results of the two kinds of measurement was thus made possible, and is effected in the following sections.

2. Reality and extent of a Si *apfu* bias in SEM-EDS analyses

As shown in Fig. A0-1, statistics of Si *apfu* from SEM-EDS analyses (calculated on an O, OH, F basis) display a shift towards values higher than 6.00, contrasting with the average 6.00 obtained from EPMA analyses.

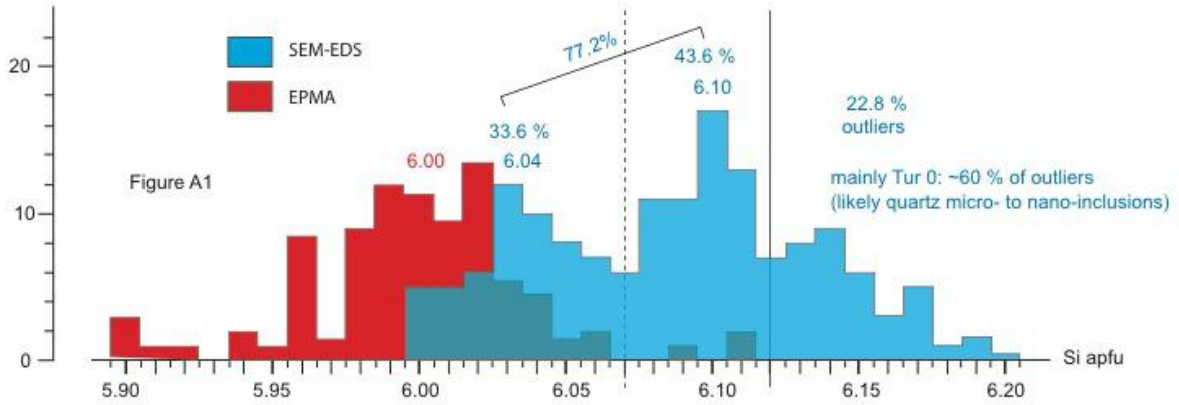

Figure A1. Comparative statistics of Si *apfu* measurements by EPMa or SEM-EDS.

More precisely, the distribution is plurimodal, and ~ 35 % are comprised between 6.0 and 6.06 (averaging 6.04), ~ 45 % are comprised between 6.06 and 6.12 (averaging 6.10) and only ~20 % are higher; the latter are named "outliers" in the following. It may also be noted that there is a consistent overlap between the EPMA distribution and the first mode of the SEM-EDS distribution: in fact, EPMA distribution could be interpreted as bimodal, with the second mode nearly coincident with the first SEM-EDS mode.

It results that ~ 80 % of the SEM-EDS analyses yield lower than 6.12 Si *apfu* values, and it may be expected that this will cause only small shifts (if any) from the EPMA reference in the various crystal chemistry diagrams: this will be addressed in the following section.

Considering the outliers, it appears that most of them (~ 60 %) come from the Tur0 relict cores. A possible explanation of such deviant analyses could be the presence in the cores of nano-inclusions of quartz crystals: as mentioned in the main text, many tourmaline crystals of the tourmalinized wall-rocks are clouded of quartz inclusions, often concentrated in the core zones. If so, the formula calculation should not affect too much the elemental ratios, and it may be expected that plotting of the analyses in the various diagrams will reveal the same trends as the "cleaner" analyses. This will be examined in a following section.

3. SEM-EPMA comparison

For the comparison, the more suitable crystals, of sufficiently large size, appear to belong to a second generation of tourmaline (Tur2), not addressed in the manuscript, of which two sets of crystals were available, in samples PAN XIX-16-a2-b1 and PAN-III-8-c1/2; in the latter, however, sufficiently contrasted zoned crystals of the first generation (Tur1) found in crack-seal quartz veinlets (see Figure 4 in main text) could also be measured by the two method, as well as late (Tur3) overgrowths on Tur2.

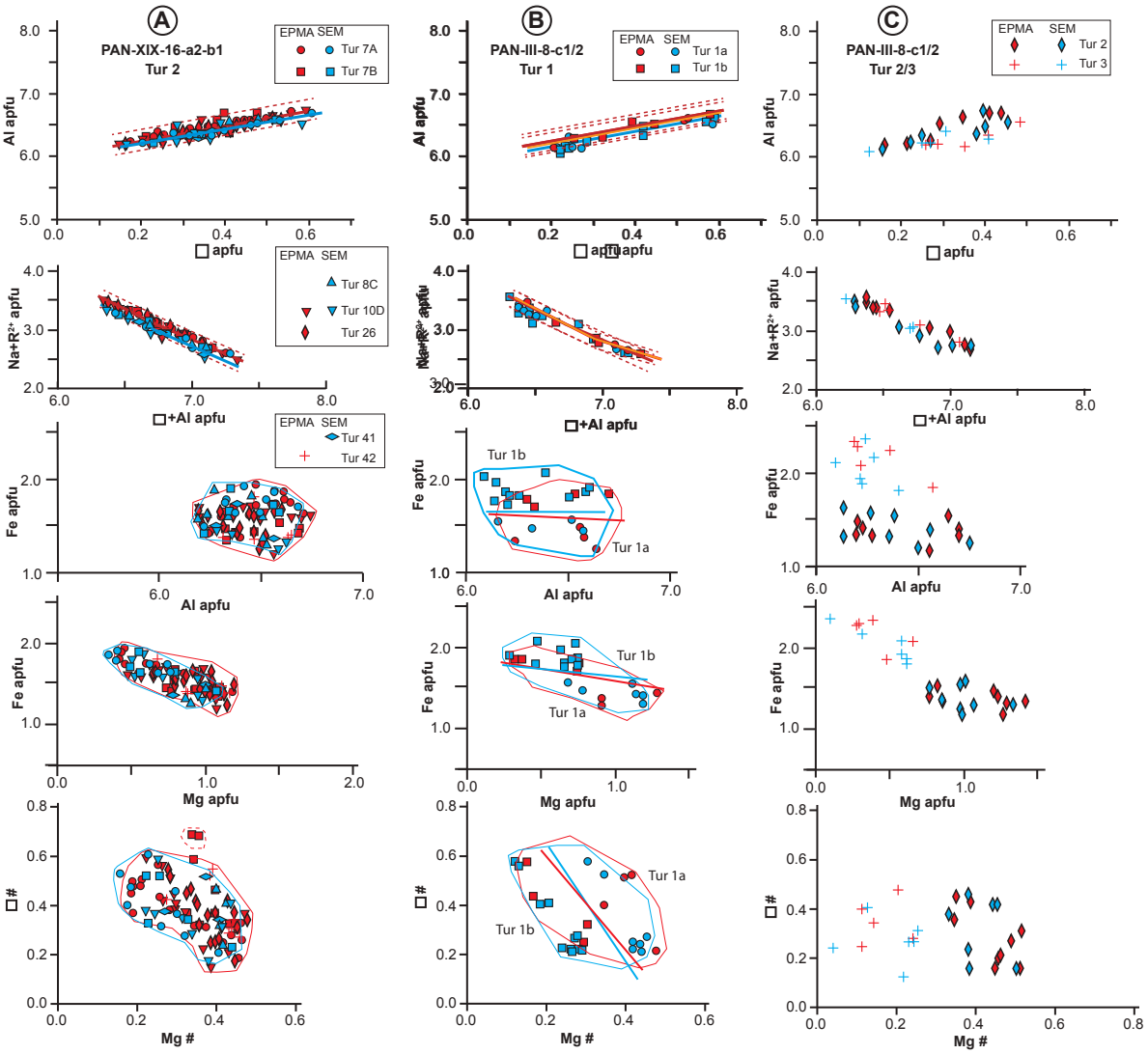

Figure A2. Comparison of EPMA and SEM-EDS measurements on selected sets of tourmaline crystals in two samples (see text).

Comparison is made in a series of diagrams in Fig. A0-2, and results are the following:

- the diagram characteristics (range of values, distribution of Tur types) are basically the same for the two sets of analyses;
- very limited shifts affect the trends in the Al vs [] and Na+R^{2+} vs Al+[] diagrams for SEM-EDS analyses relative to EPMA ones: nevertheless, the SEM-EDS trends remain included in the dispersion field of EPMA analyses;
- the Al/Fe/Mg ratios seem in particular identical in the two sets of results; this is confirmed by examination of the AFM diagrams in Fig. A0-3. It is noteworthy that the dispersion of the Al/Fe+Mg ratios is similar whatever the analysis method, thus certifying that this dispersion is real.

It may thus be concluded that use of SEM-EDS analyses in place of EPMA ones for the considered crystals did not affect the restitution of crystal chemistry properties.

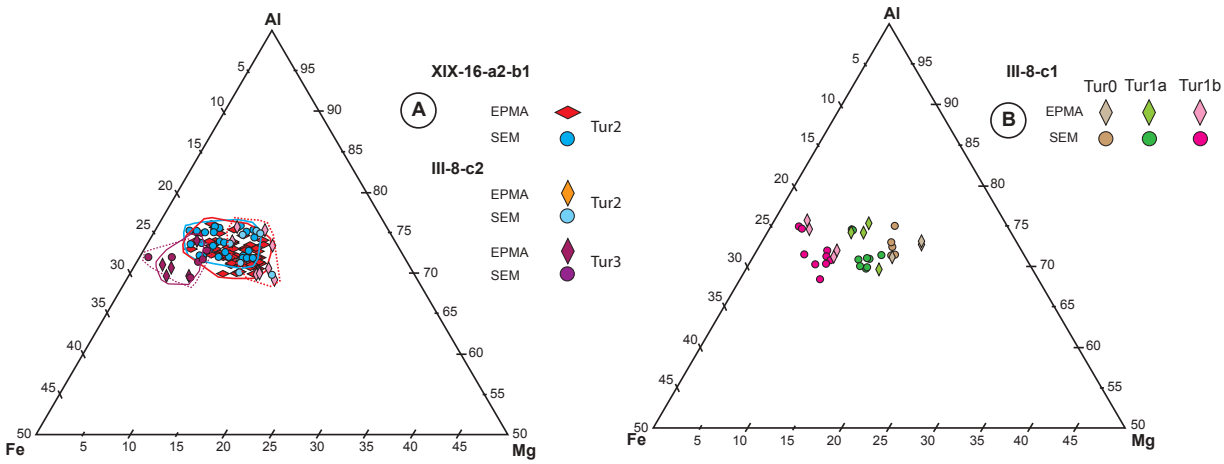

Figure A3. Comparison of EPMA and SEM-EDS analyses in AFM diagrams. **A**: Tur2 (samples PAN-XIX-16-a2-b1 and PAN-III-8-c2) and Tur3 (PAN-III-8-c2; **B**: Tur 0 and Tur 1 (sample PAN-III-8-c1, excepted Tur0-EPMA, taken from other samples).

4. Internal consistency of SEM-EDS analyses

Separating the analyses in three sets corresponding to the three modes in Fig. A0-1 (mode 1 = "low" Si, mode 2 = "high" Si, mode 3 ="outliers") is done in the diagrams of Fig. A0-4 and

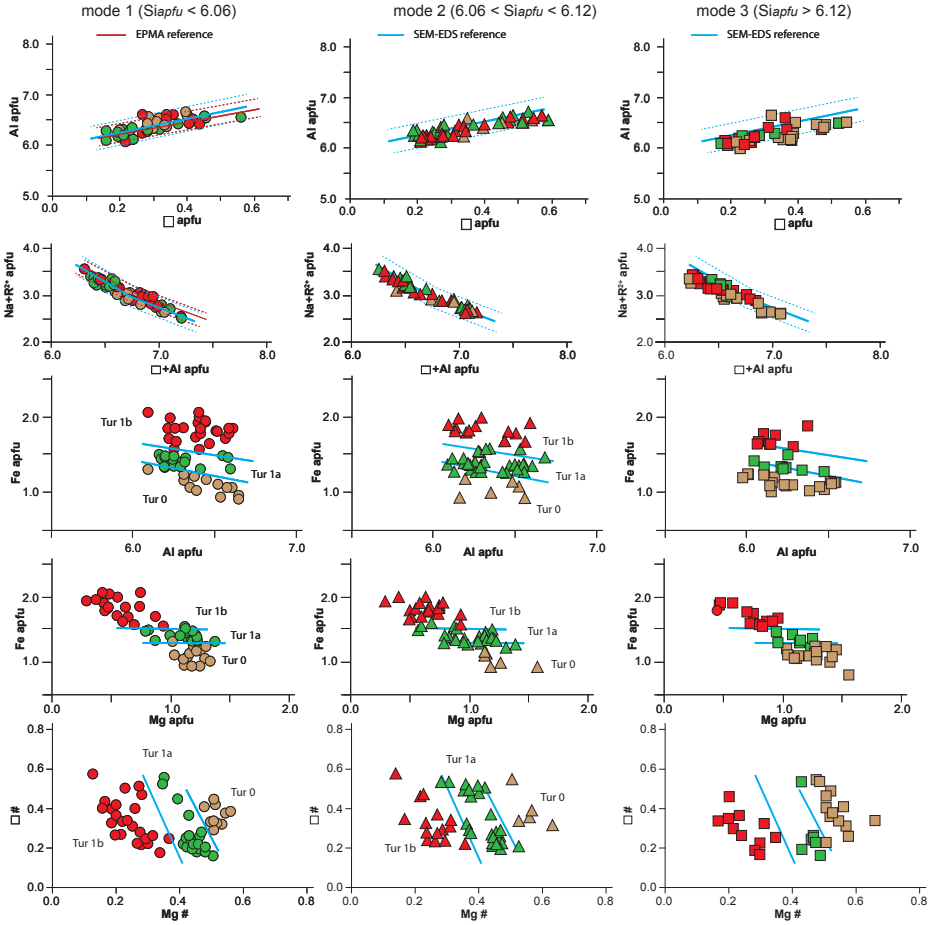

Figure A0-4. Checking the internal consistency of SEM-EDS analyses using classical crystal chemistry diagrams. The domain boundaries are those corresponding to mode 1 in all diagrams. The red lines correspond to EPMA reference.

A0-5.

(i) A first result is that in the Al vs [] and Na+R^{2+} vs Al+[] diagrams, the whole of the mode 1 values behave as the ones in sample III-8-c, as indeed expected. The crystal chemistry diagrams of these mode 1 analyses may thus be in turn used as reference for the other sets of analyses.

(ii) In all the diagrams, the mode 2 values yield basically the same relations, and in particular, the boundaries between "Tur0", "Tur1a" and "Tur1b" fields are very consistent in the three Fe vs. Al, Fe vs Mg and []# vs. Mg# diagrams in Fig. A0-4, and in the AFM diagrams in Fig. A0-5.

(iii) As expected, the "outlier" values are shifted in the Al vs [] and $Na+R^{2+}$ vs Al+[] diagrams, displaying nevertheless the same characteristics. They however are highly compatible with the preceding sets of values in the other diagrams. This is particularly significant for the Tur0 values.

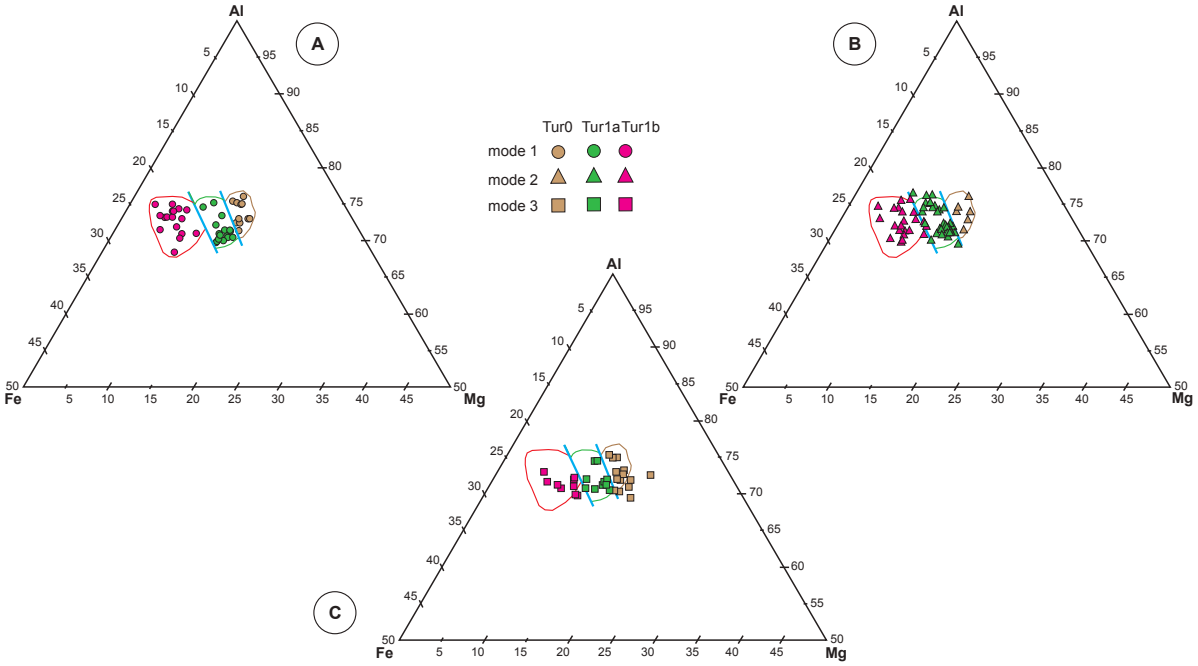

Figure A0-5. Checking the internal consistency of SEM-EDS analyses in the AFM triangle. **A**: mode 1 ("low Si"); **B**: mode 2 ("high" Si); **C**: mode 3 ("outliers"). The domain boundaries are those corresponding to mode 1 in all three diagrams.

5. The case for F

It is known that, in tourmaline, there may be a rough linear relationships between F content and the ionic charge associated with the site X infilling. Consideration of Fig. A0-6 shows that this is indeed the case and that:

- (i) there is no significant differences between the SEM-EDS analyses corresponding to either mode 1, or mode 2 or mode 3 of the Si distribution (Fig. A0-6A to C)
- (ii) the scarcity of EPMA measurements in Tur 1 prevents a comparison zone by zone, although the rare Tur0 measurements by EPMA confirm that F content in Tur0 id generally low (Fig. A0-6A)
- (iii) if therefore EPMA and SEM-EDS analyses are considered as a whole (Fig. A0-6D and E), both sets of analyses display a large dispersion and a very rough linear relationship, with a slight difference between the two sets which nevertheless does not introduce a significant difference for the data interpretation.

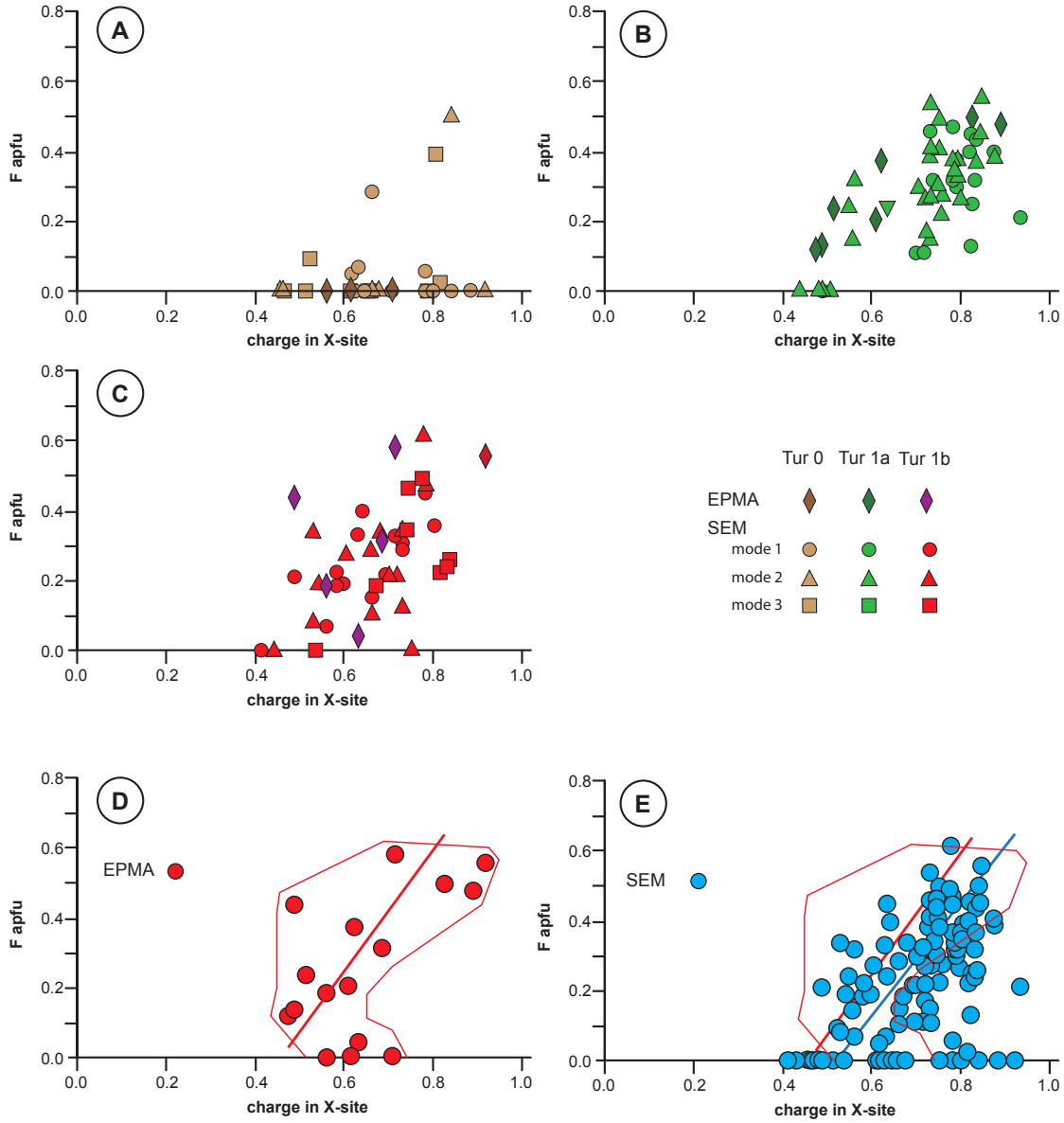

Figure A0-6. Relationships between F and the X-site charge: comparison of EPMA and SEM-EDS results. **A** to **C**: comparison zone by zone (**A**: Tur0; **B**: Tur 1a; **C**: Tur 1b); **D**-**E**: bulk comparison. Contours in E: from D

6. Conclusion

It results from the preceding that the SEM-EDS analyses may be safely used for the crystal chemistry characterization of the Panasqueira tourmaline, provided that analyses from mode 3 group be discarded.

Finally, 117 spots in 19 samples are taken into consideration in the main text.

1284 **Appendix A1-Table A1: Operating conditions for the LA-ICP-MS equipment**

Laboratory & Sample Preparation	
Laboratory name	Géosciences Rennes, UMR CNRS 6118, Rennes, France
Sample type/mineral	Rutile
Sample preparation	Rutile grains in context in thin-sections
Imaging	JEOL J7600F scanning electron microscope (SEM)
Laser ablation system	
Make, Model & type	ESI NWR193UC, Excimer
Ablation cell	ESI NWR TwoVol2
Laser wavelength	193 nm
Pulse width	< 5 ns
Fluence	8.0 J/cm-2
Repetition rate	5 Hz
Spot size	45 µm (round spot)
Sampling mode / pattern	Single spot
Carrier gas	100% He, Ar make-up gas and N2 (3 ml/mn) combined using in-house smoothing device
Background collection	20 seconds
Ablation duration	60 seconds
Wash-out delay	15 seconds
Cell carrier gas flow (He)	0.75 l/min
ICP-MS Instrument	
Make, Model & type	Agilent 7700x, Q-ICP-MS
Sample introduction	Via conventional tubing
RF power	1350W
Sampler, skimmer cones	Ni
Extraction lenses	X type
Make-up gas flow (Ar)	0.87 l/min
Detection system	Single collector secondary electron multiplier
Data acquisition protocol	Time-resolved analysis
Scanning mode	Peak hopping, one point per peak
Detector mode	Pulse counting, dead time correction applied, and analog mode when signal intensity > ~ 10^6 cps
Masses measured	^{204}(Hg + Pb), ^{206}Pb, ^{207}Pb, ^{208}Pb, ^{232}Th, ^{238}U
Integration time per peak	10-30 ms
Sensitivity / Efficiency	25000 cps/ppm Pb (50µm, 10Hz)
Dwell time per isotope	5-70 ms depending on the masses
Data Processing	
Gas blank	20 seconds on-peak
Calibration strategy	R10 Rutile used as primary reference material, R19 rutile used as secondary reference material (quality control)
Reference Material info	R10 (Luvizotto et al., 2009) R19 (Zack et al., 2011)
Data processing package used	Iolite (Paton et al., 2010), VizualAge_UcomPbine (Chew et al., 2014)
Quality control / Validation	R19: Apr 2016: 490 ± 3.4 Ma (MSWD=1.11; N=13) Dec 2017 : 493 ± 12 Ma (MSWD=2; N=12)

1285
1286

Appendix A2: Ar-Ar dating of muscovite (methodology)

Argon isotopes (from mass 40 to 37) were measured using Faraday detectors with low noise 1 x 10^{12} Ω resistors and mass 36 was measured using a compact discrete dynode (CDD) detector. The sensitivity for argon measurements is ~6.312 x 10^{17} moles/fA as determined from measured aliquots of Fish Canyon Sanidine (Dazé et al., 2003; Kuiper et al., 2008). Standards and sample were placed in 2 mm deep wells in 18 mm diameter aluminium disks, with standards placed strategically so that the lateral neutron flux gradients across the disk could be evaluated. Planar regressions were fit to the standard data, and the $^{40}Ar/^{39}Ar$ neutron fluence parameter (J) interpolated for the unknowns. Uncertainties in J are estimated at 0.1 - 0.2% (1 σ), based on Monte Carlo error analysis of the planar regressions (Best et al., 1995). All specimens were irradiated in the Cadmium-lined, in-core CLICIT facility of the TRIGA reactor at the Oregon State University (USA). The duration of irradiation was 17 hours and using the Fish Canyon sanidine (Kuiper et al., 2008) and GA1550 biotite (Spell and McDougall, 2003) standards. Standards for $^{40}Ar/^{39}Ar$ measurements were placed in a Cu sample tray, with a KBr cover slip, in a stainless steel chamber with a differentially pumped ZnS viewport attached to a Thermo Fisher Scientific extraction/purification line and baked with an infrared lamp for 24 hours. Single crystals were fused using the CO_2 laser. The sample selected for the $^{40}Ar/^{39}Ar$ dating has been previously investigated by optical microscopy and SEM in order to spot homogeneous areas devoid of alteration, micro-inclusions or internal zoning. Discs of 5 mm in diameter and ~150 µm thick were cut from the same polished thick section (150 - 200 µm thick). The discs were mounted using a ceramic adhesive (PELCO) on a quartz slide placed in a stainless steel chamber with a sapphire viewport attached to the same stainless steel high vacuum extraction system as the CO_2 laser, and baked with an infrared lamp for 48 hours. For this study, a raster size of about 100 x 100 µm was used and ablation pits were excavated to an estimated depth of 50 µm. Reactive gases were removed for both the standard and unknown, after 3 minutes, by three GP-50 SAES getters (two at room temperature and one at 450 °C) prior to being admitted to an ARGUS VI mass spectrometer by expansion. Five argon isotopes were measured simultaneously over a period of 6 minutes.

References cited

Best, M.G., Christiansen, E.H., Deino, A.L., Grommé, C.S., and Tingey, D.G., 1995, Correlation and emplacement of a large, zoned, discontinuously exposed ash-flow sheet: Ar/ Ar 40 39 chronology, paleomagnetism, and petrology of the Pahranagat Formation, Nevada: Journal of Geophysical Research, v. 100, p. 24,593-24,609.

1321 Dazé, A., Lee, J.K.W., and Villeneuve, M., 2003, An intercalibration study of the Fish Canyon
1322 sanidine and biotite $^{40}Ar/^{39}Ar$ standards and some comments on the age of the Fish Canyon
1323 Tuff: Chemical Geology, v. 199, p. 111–127.
1324 Kuiper, K.F., Deino, A., Hilgen, F.J., Krijgsman, W., Renne, P.R., and Wijbrans, J.R., 2008,
1325 Synchronizing the rock clocks of Earth history: Science, v. 320, p. 500–504.
1326 Spell, T.L., and McDougall, I., 2003, Characterization and calibration of $^{40}Ar/^{39}Ar$ dating standards:
1327 Chemical Geology, v. 198, p. 189–211..
1328

Appendix A8: Mass balance calculations

Boron mass balance calculations

Boron endowment in the granites: It must be emphasized that the greisenized cupola and the subjacent granites layer are typically devoid of tourmaline, meaning that the original melts were not tourmaline saturated. This raises the question of these granites being a boron source for the Panasqueira system. In any case, these granites being of the RMG family, and their solidus temperature being accordingly in the c. 600°-650°C range (Aksyuk and Konyshev, 2011), their boron content could not have been higher than the equilibrium B content in equilibrium with tourmaline in the melt at these temperatures, i.e., no more than 0.5 wt% B_2O_3 (London, 2011; and references therein). The volume of the cupola itself (approximated by a cone, high 150 m, diameter 250 m) being of ~ $2.5.10^6$ m^3, it could not contain more than ~9 kt B (with a melt density of 2.3 $t.m^{-3}$: Dingwell et al., 1993). The subjacent RMG sheet-like body, made of several separate intrusions (De Amorin, 2017), may be approximated as a 100 m thick body with about 1 km^2 surface (Fig. 2), yielding a ~ 10^8 m^3 volume and a maximal content of 360 kt B. Thus, the total possible boron yield by the evolved granites could not have exceeded 370 kt B.

Boron required for the wall-rock tourmalinization: These values must be compared with the B content in the tourmalinized wall-rock. (i) At the single vein scale, we consider an average vein system based onto the description by Foxford et al. (2000, their Fig.8): an elliptical area (minor axis ~100 m, major axis ~300 m), a total width of the tourmalinized margins of 0.45 m (i.e., 15 cm on one side of the vein and 30 cm on the other) and an averaged 50 volume % of tourmaline in the altered zones. This yields a unitary volume of the altered zone of ~ $1.1.10^4$ m^3. Adopting an average density of 3.1 $t.m^{-3}$, and a boron content of 3.3% for the tourmaline, this unitary volume contains ~ 540 t B. (ii) The number of elementary veins may be estimated using the published values for the total volume of the vein system, between 3 and 6.10^{-3} km^3 (Polya, 1989), and assuming an average vein thickness of 0.2 m (Foxford et al., 2000). This yields an estimated number of elementary veins comprised between 750 and 1500. (iii) Finally, the total B content of the tourmalinized wall rocks may be bracketed between 410 and 810 kt. These values are clearly higher than the maximum boron tonnage possibly delivered by the Panasqueira RMG.

Volume of magmatic water required for boron transportation

At the elementary vein scale, and at any time of the tourmalinization process, the effective volume of fluid present in the V_0 volume of altered rocks (estimated at $1.2.10^4$ m^3, see above) is controlled by rock porosity. If ϕ is the porosity, this effective volume is only $\phi.V_0$. The porosity of

metamorphic rocks is generally considered to be in the 10^{-1} to 10^{-2} range (Bickle and McKenzie 1987), and was for instance estimated at 0.08 in the Tinos schists (Breeding et al., 2003). Here, we take ϕ=0.1. The effective $\phi.V_0$ volume contains a boron mass $m_0 = \phi.V_0.\rho_w.X$, with ρ_w the fluid density and X the boron content in the fluid. For a magmatic fluid equilibrated with tourmaline at the solidus temperature, the boron content X will be close to 1 wt % B_2O_3 (Weisbrod et al., 1986) and the fluid density will be in the 0.62-0.68 $t.m^{-3}$ range, depending on salinity between ~ 10 and ~ 20 wt% NaCl (Sakuma and Ichiki, 2016); taking an average 0.65 yields m_0= 2 t B. Therefore, to attain the 540 t B accumulated in the tourmalinized wall rock, the $\phi.V_0$ volume must be renewed 540/2=270 times, i.e., a total flow of $270.\phi.V_0 = 2.9.10^6$ m^3 of fluid must be channelled through the transforming schist. At the deposit scale, this in turn means that a volume of fluid comprised between $2.2.10^9$ and $4.3.10^9$ m^3 was required for the tourmalinization be effective.

Possible water yield by the granite system

The water content of a RMG melt is ~ 5 wt%. Thus, the Panasqueira RMG sheet-like body, with a volume of 10^8 m^3 and a melt density of 2.3 $t.m^{-3}$, contained about $1.2.10^7$ t water, i.e. (with a water density of 0.65 $t.m^{-3}$) could have expelled ~ $1.8.10^7$ m^3 of fluid. This is clearly two orders of magnitude below the required fluid quantity. It must be noted that it is the same for the main wolframite deposition stage, as already stated by Polya (1989), who estimated a several 100 km^3 (up to 1000) flow to produce the deposit. This was however based on a 0.2 ppm W content in the fluid, which was clearly underestimated: owing to the data of Wood and Vlassopoulos (1989), a content of ~ 500 ppm W is more realistic, and would demand a volume of ~ 5.10^8 m^3 to yield the c. 150 kt of W of the deposit, one order of magnitude larger than the granite water endowment.

Metasediments as a source of boron and fluid

The Beira schists contain in average ~ 100 ppm B (Oosterom et al., 1984). With this content, and assuming a density for the schist of 2.77 t.m-3 (Ribeiro, 2017), a schist volume of 1.7 km^3 to 3.4 km^3 is required, admitting a 100% efficient extraction, which is not so likely. However, the few data available for the high grade Beira schists (Peña Negra migmatitic complex, Acosta-Vigil et al., 2011) suggest that boron extraction may have reached 70% efficiency. With this value, the needed volumes become comprised between 2,8 km^3 and 4,8 km^3. On the other hand, to yield the volume of fluid required by the boron transportation and deposition (see above), assuming a water productivity of about 3 wt % (Fyfe et al., 1978), between 20 km^3 and 40 km^3 of schist are necessary. The source of boron and fluids for the tourmalinization at Panasqueira could therefore have been the Beira schists.

1397 *References cited*

1398 Acosta-Vigil, A., Pereira, M.D., Shaw, D.M., and London, D., 2011, Contrasting behaviour of
1399 boron during crustal anatexis: Lithos, v. 56, p. 15-31.

1400 Bickle, M.J., and McKenzie, D., 1987, The transport of heat and matter by fluids during
1401 metamorphism: Contributions to Mineralogy and Petrology, v. 95, p. 384-392.

1402 Breeding, C.M., Ague, J.J., Brocker, M., and Bolton, E.W., 2003, Blueschist preservation in a
1403 retrograded, high-pressure, low-temperature metamorphic terrane, Tinos, Greece:
1404 implications for fluid flow paths in subduction zones: Geochemistry Geophysics Geosystems,
1405 v. 4, 1: 9002, doi: 10.1029/2002GC000380.

1406 De Amorin, A., 2017, Pétrographie géochimie des granitoides de la mine de W de Panasqueira
1407 (Portugal): Rôle dans la genèse des minéralisations: Unpublished M.Sc. thesis, Université de
1408 Lorraine (France), Laboratoire Géoressources, 37 p.

1409 Dingwell, D.B., Knoche, R., and Webb, S.L., 1993, The effect of F on the density of haplogranite
1410 melt: Amererican Mineralogist, v. 78, p. 325-330.

1411 Foxford, K.A., Nicholson, R., Polya, D.A., and Hebblethwaite, R.P.B., 2000, Extensional failure
1412 and hydraulic valving at Minas da Panasqueira, Portugal: evidence from vein spatial
1413 distributions, displacements and geometries: Journal of Structural Geology, v. 22, p. 1065–
1414 1086, http://dx.doi.org/10.1016/S0191-8141(00)00029-8.

1415 Fyfe, W.S., Price, N.J., and Thompson, A.B., 1978, Fluids in the earth's crust. Amsterdam: Elsevier,
1416 389 p.

1417 Oosterom, M.G., Bussink, R.W., and Vriend, S.P., 1984, Lithogeochemical studies of aureoles
1418 around the Panasqueira tin-tungsten deposit, Portugal: Mineralium Deposita, v. 19, p. 283-
1419 288.

1420 Polya, D.A., 1989, Chemistry of the main-stage ore-forming fluids of the Panasqueira W–Cu(Ag)–
1421 Sn deposit, Portugal: implications for models of ore genesis: ECONOMIC GEOLOGY, v. 84,
1422 p. 1134–1152.

1423 Ribeiro, R.F., 2017, Gravimetric Modelling and Geological Interpretation of Argemela-Panasqueira
1424 Area: PhD Thesis, Porto Universidad, 61 p.

1425 Sakuma, H., and Ichiki, M., 2016, Density and isothermal compressibility of supercritical H_2O-
1426 NaCl fluids: molecular dynamics study from 673 to 2000 K, 0.2 to 2 GPa, and 0 to 22 wt%
1427 NaCl: Geofluids, v. 16, p. 89-102.

1428 Weisbrod, A., Polak, C., and Roy, D., 1986, Experimental study of tourmaline solubility in the
1429 system Na–Mg–Al–Si–B–O–H. Applications to the boron content of natural hydrothermal

1430 fluids and tourmalinization processes: International Symposium on Experimental Mineralogy
1431 and Geochemistry (Nancy), Abstracts, v. 140-141.
1432 Wood, S.A., and Vlassopoulos, D., 1989, Experimental determination of the solubility and
1433 speciation of tungsten at 500 °C and 1 kbar: Geochimica et Cosmochimica Acta, v. 53, p.
1434 303–312.